

Modelling the Evolution of Elliptical Röhliberger Channels

Isaac BROWN^{1*}, Katarzyna L. P. Warburton¹, Jerome A. Neufeld^{1,2,3}

¹Department of Applied Department of Applied Mathematics and Theoretical Physics, University of Cambridge, Cambridge, UK

²Department of Earth Sciences, University of Cambridge, Cambridge, UK

³Institute for Energy and Environmental Flows, University of Cambridge, Cambridge, UK

*Correspondence: Isaac Brown (ipb28@cam.ac.uk)

Email addresses

K. L. P. Warburton: (klpw3@cam.ac.uk)

J. A. Neufeld (jn271@cam.ac.uk)

Manuscript Statement: This paper is a non-peer reviewed pre-print submitted to EarthArXiv. This work has been submitted to the Journal of Glaciology for peer review.

Modelling the Evolution of Elliptical Röthlisberger Channels

Isaac BROWN,¹ Katarzyna L. P. Warburton,¹ Jerome A. Neufeld,^{1,2,3}

¹*Department of Applied Mathematics and Theoretical Physics, University of Cambridge, Cambridge, UK*

²*Department of Earth Sciences, University of Cambridge, Cambridge, UK*

³*Institute for Energy and Environmental Flows, University of Cambridge, Cambridge, UK*

Correspondence: Isaac Brown <ipb28@cam.ac.uk>

ABSTRACT. Subglacial water flow is critical to basal sliding and ice dynamics. Modelling the coupled evolution of subglacial drainage and ice flow remains challenging, however. This study investigates the evolution of the basal ice-water interface by analysing heat and fluid flow in idealised englacial channels. We extend the classical R othlisberger model for circular channels to elliptical channel geometries. A hybrid laminar–turbulent melt scheme captures heat generation and melting from both viscous and turbulent dissipation, while a viscous flow law models the creep closure of the surrounding ice. Whilst the flow of ice tends to increase the eccentricity of the channel, we find that elliptical channels tend toward a circular shape when laminar melting dominates due to differential melting between the roof and walls of the channel. Our hybrid melt model predicts the existence of stable, non-circular cross-sections. Unlike circular channels, these channels obey pressure–flux relationships that, beyond a critical volume flux threshold, suggest a preference for flux sharing, a behaviour characteristic of distributed drainage networks. This contrasts with circular channels, which undergo channelisation towards fewer, larger conduits. These idealised channels suggest potential simplifications to modelling subglacial drainage networks and the dynamics of evolving subglacial hydrological networks.

27 **INTRODUCTION**

28 Greenland and Antarctica are the world's largest store of freshwater ice, with the potential to become
29 the main drivers of sea-level rise (Mouginot and others, 2019; DeConto and Pollard, 2016). Subglacial
30 water plays a key role in determining how the ice sheets slide over their bases, and hence how much ice is
31 transported to regions where melting is enhanced — the ocean or lower altitudes (Schoof, 2010; Hewitt, 2013;
32 Bougamont and others, 2014; Iken and Bindschadler, 1986; Clarke, 1987; Flowers, 2015). Yet, ice-sheet-scale
33 models struggle to include dynamic subglacial hydrology (Flowers, 2015; Kazmierczak and others, 2024;
34 Sommers and others, 2018), resulting in uncertainties in sea-level rise predictions (Zoet and Iverson, 2020;
35 Pörtner and others, 2019; Feldmann and Levermann, 2015). Although the most sophisticated models now
36 attempt to include some drainage elements (e.g. channels) (e.g. Sommers and others, 2024; De Fleurian and
37 others, 2018; Ehrenfeucht and others, 2025), due to the large range of length scales involved, 1 m to 10^5 m,
38 ongoing work is needed to find a consistent physical model that describes these subglacial and englacial
39 networks (Warburton and others, 2024), which can then be upscaled or implemented in ice-sheet-scale
40 simulations.

41 At the base of glaciers and ice sheets, sufficiently large flows of water are observed to carve out channels,
42 which are significant conduits of meltwater to the ocean. Röthlisberger was the first to posit that at
43 every cross-section of a drainage channel, there exists a local balance between outward melting of the
44 channel walls and the inward viscous collapse of the surrounding ice — as much ice is melted as flows in
45 (Röthlisberger, 1972; Walder, 2010). Viscous dissipation (frictional heating) in the flowing water causes melt
46 of the ice-water boundary, while the viscous flow of ice due to overburden stresses drives channel collapse
47 or closure. Röthlisberger's model assumed a circular cross-section for the channel, which allowed the use
48 of Nye's analytic expression to describe the closure rate of the channel (Nye, 1953). In this formulation,
49 the closure rate is driven by the effective pressure, N , defined as the difference between the ice overburden
50 pressure, p_i , and the water pressure within the channels, p_w ($N = p_i - p_w$). Conversely, the melting power
51 is given by the product of the volumetric flux, q , and the pressure gradient, G . The theoretical treatment
52 of these variables involves a distinction in regard to the primary external drivers: while Röthlisberger's
53 analysis focuses on the steady-state relationship between N and q , later extensions by Walder and Fowler
54 (1994) and Ng (2000) emphasise G as a largely constant driver dictated by the regional ice-surface slope
55 and bed topography. Using this model, Röthlisberger derived relationships between pressure gradients

56 driving the flow and the resulting volumetric flow rates, providing evidence of subglacial water preferentially
57 flowing in larger channels than in distributed, sheet-like flow. Walder and Fowler (1994) and subsequently
58 Ng (2000) expanded this framework to account for other subglacial drainage elements — notably canals
59 incised into deformable subglacial sediment — with fundamentally different pressure-flux relationships.

60 Theoretical investigations into non-circular englacial and non-semicircular subglacial channels have been
61 motivated by observational evidence and model predictions. Water pressures in subglacial channels are
62 frequently observed to be higher than reasonably predicted by circular channels (Iken and Bindshadler, 1986;
63 Hooke and others, 1990), and more recent direct observations of non-circular channel cross-sections with
64 large aspect ratios have been made (Kamintzis and others, 2023; Church and others, 2020). Furthermore,
65 many sophisticated subglacial network models break down for very thin and tall channels and predict
66 ever-narrowing channels, suggesting an underlying drive towards more eccentric cross-sections (Hewitt, 2011;
67 Sommers and others, 2018).

68 Motivated by higher-than-previously-predicted observed water pressures, Hooke and others (1990)
69 modelled subglacial channels as low and broad (the arc of a circle forming the ice ceiling and its chord as
70 the bedrock base). This new channel shape required higher pressure gradients to drive the same amount
71 of flux, providing an explanation for the higher water pressures. Fowler and Ng (1996) considered a
72 subglacial channel cross-section in the shallow limit of great width and very low ceilings — the ice-roof and
73 bedrock-bottom boundaries were treated as parallel. More recent models have been proposed for non-circular
74 cross-sections due to variations in the viscous collapse of the ice. Meyer and others (2016) showed that
75 initially circular channels can be deformed into either broader or taller channels due to anti-plane shearing
76 within the ice, for example, near shear margins or under surging glaciers. If the ice surrounding a channel
77 experiences shearing (vertical or horizontal variation in the downstream velocity) there is a local variation in
78 the viscosity of the ice causing an initially circular or semicircular channel to deform. Dallaston and Hewitt
79 (2014) considered the stability and shape evolution of channels without making any *a priori* assumptions
80 about their cross-sections. By approximating the ice rheology as Newtonian and modelling the meltwater as
81 a uniform heat source that filled the cavity, they demonstrated that the simple contraction of a circular cavity
82 is unstable to perturbations in the channel shape, and instead ellipses provide an exact and stable solution,
83 provided their aspect ratios are sufficiently close to unity. Though their work provides a framework to
84 better understand the observational evidence of non-circular channel cross-sections, they note the limitation
85 of their uniform heating model and speculate that non-uniform melting along the interface, due to its

86 geometry, may result in new stable, non-circular cross-sections.

87 In this work, we model the flow of water through the channels to derive a spatially variable melt rate
88 along the perimeter of the channels' ice-water interface. Furthermore, we extend R othlisberger's model to
89 include elliptical channels, which allows for a variation in the aspect ratio of the channels. We consider
90 melting caused by both laminar and turbulent flow and introduce a hybridised laminar–turbulent melt
91 model, resulting in stable elliptical cross-sections. We examine the resulting pressure-flux relationships of
92 these stable channels, revealing that channels with elliptical cross-sections, beyond a critical flux threshold,
93 tend to share flux, similar to that of a distributed drainage network. This behaviour contrasts with circular
94 channels, which undergo channelisation towards fewer, larger channels. Finally, the implications and
95 limitations of this work are discussed in the broader context of ice flow models.

96 MATHEMATICAL MODEL AND APPROACH

97 We consider an elliptical englacial channel that is uniform in the along-flow (x) direction and is connected
98 to a water source providing a constant volume flux to the channel. We assume that the channel grows in
99 cross-section only due to melt-back of the ice, driven by viscous dissipation in the flow of water that fully
100 fills the channel. The viscous dissipation in the flow produces a temperature profile which is then used to
101 calculate a spatially-varying melt rate along the channel wall. We further assume that the channel closure
102 is due only to the viscous collapse of the surrounding ice, which is modelled using Newtonian Stokes flow.

103 We first consider the limit of laminar flow in the channel and subsequently consider turbulent flow.
104 Thereafter, we find the temperature profile for the laminar and separately the turbulent flow, before
105 considering the resulting melt at the ice-water boundary. We then bring together the two types of melting
106 by proposing a hybrid laminar–turbulent melting scheme, which captures flow in small and large channels,
107 and ones with high aspect ratios. This hybrid melting is combined with the viscous collapse of the channel
108 to determine stable cross-sectional aspect ratios and areas.

109 Flow Through the Channel

110 The flow in the channel is driven by a pressure gradient, $G \equiv -dp/dx$, with a constant input volume-flux, q .
111 We assume gravity plays a negligible role in determining the flow inside the channel, and that a quasi-steady
112 state exists where the interface melts back slowly with the flow adjusting quickly to new cross-sections
113 so that a time-independent description is sufficient. We assume the water, with viscosity η_w , experiences

114 a no-slip condition at the channel boundary. The channel is restricted to the shape of an ellipse with
 115 horizontal semi-axis, a , and vertical semi-axis, b , in the y and z -directions, respectively; see Fig. (1). We
 116 define its aspect ratio as $\xi = b/a$. Ω denotes the interior of the ellipse with an area, $A = \pi ab$, and $\partial\Omega$ defines
 117 its boundary.

118 *Laminar Flow*

119 For small channels with little volume flux, the flow is laminar and unidirectional and the Reynolds number,

$$\text{Re} = \frac{\rho_w U L}{\eta_w}, \quad (1)$$

120 where ρ_w denotes the density of water and U and L are the characteristic velocity and length scales, is
 121 small. In the limit $\text{Re} \ll 1$, this flow is described by the Stokes equation,

$$\nabla^2 u = -\frac{G}{\eta_w} \quad \text{in } \Omega, \quad (2)$$

$$u = 0 \quad \text{on } \partial\Omega. \quad (3)$$

122 This has a known solution (Happel and Brenner, 1983) for the water velocity

$$u = \frac{Ga^2b^2}{2\eta_w(a^2 + b^2)} \left(1 - \frac{y^2}{a^2} - \frac{z^2}{b^2} \right), \quad (4)$$

123 which we use to find the volumetric flux,

$$q = \frac{G}{4\pi\eta_w} \frac{\xi}{\xi^2 + 1} A^2, \quad (5)$$

124 written here in terms of the cross-sectional area A and the aspect ratio ξ of the channel. Fig. (2a) shows
 125 the scaled flow field through a channel with an aspect ratio of $\xi = 1/2$.

126 These descriptions may be made non-dimensional, and we choose to scale both these solutions and
 127 subsequent turbulent and hybrid solutions in the following way. The dimensions of the ellipse are scaled
 128 differently in the two principal directions, $y \sim a$ and $z \sim b$, and the velocity is scaled by the average flow
 129 speed $u \sim u_{av} = q/A$. The scaled boundary is therefore a circle

$$\tilde{y}^2 + \tilde{z}^2 = 1, \quad (6)$$

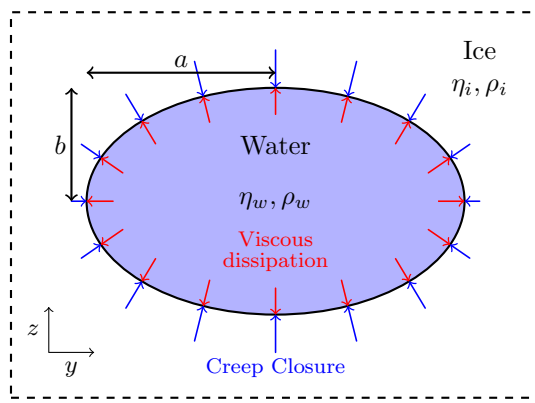


Fig. 1. Schematic representation of an elliptical englacial channel: The water flows into the page and is surrounded by ice. The red outward normal arrows represent melting driven by viscous dissipation, and the blue varying inward normal arrows represent the collapse due to viscous collapse of the surrounding ice.

130 and the scaled Poisson equation, (3), describing the flow in the channel becomes

$$\xi^2 \frac{\partial^2 \tilde{u}}{\partial \tilde{y}^2} + \frac{\partial^2 \tilde{u}}{\partial \tilde{z}^2} = -4(\xi^2 + 1), \quad (7)$$

131 which has solution

$$\tilde{u} = 2(1 - \tilde{y}^2 - \tilde{z}^2). \quad (8)$$

132 The geometric influence of the elliptical cross-section for laminar flow can therefore be entirely accommodated
133 by the rescaling of the principal axes and the introduction of ξ to the governing equation. This scaling and
134 notation facilitate the subsequent analysis of the temperature field.

135 *Turbulent Flow*

136 In the turbulent limit, we expect a non-linear relation between the volume flux and the applied pressure
137 gradient. We can show this by arguing that the mean turbulent flow U is surrounded by a thin laminar
138 boundary layer of width δ along the perimeter, P , of the channel cross-section, see Fig. (2b). The width
139 of the boundary layer can be approximated by assuming that the local Reynolds number at the laminar
140 boundary is at its critical value,

$$\text{Re}_c = \frac{\rho_w U \delta}{\eta_w} \simeq 10^3. \quad (9)$$

141 The resistive force to bulk flow is assumed to be from the viscous boundary layer only $\sim P\eta_w U/\delta$. The
142 water flows due to the force from the pressure gradient acting across the entire cross-sectional area A .

143 Balancing the driving and resistive forces gives

$$\eta_w \frac{U}{\delta} P \simeq GA. \quad (10)$$

144 If we rearrange this expression and substitute for the boundary layer width we find that

$$G = \frac{1}{\text{Re}_c} \frac{P}{A} \rho_w U^2. \quad (11)$$

145 This is equivalent to the empirically derived Darcy-Weisbach equation (Weisbach, 1850),

$$G \equiv -\frac{dp}{dx} = f_D \frac{\rho_w U^2}{2D_H}, \quad (12)$$

146 where, by convention, $D_H \equiv 4A/P$ is termed the hydraulic diameter and $f_D \sim 1/\text{Re}_c$ is the friction factor.
 147 We note, in general, that the value of f_D in the turbulent limit depends on several factors including, for
 148 example, the relative roughness of the channel. Here we shall assume that $f_D \sim 10^{-3}$ as in Hewitt and
 149 others (2018). It is possible to define a friction factor in the laminar case, and then go on to combine the
 150 flow regimes into a hybridised flow scheme using a friction factor that depends on the Reynolds number, see
 151 for example (Churchill, 1977; Hewitt and others, 2018). We refrain from doing so here, because a hybrid
 152 flow formulation is unable to resolve the variations in heat flux along the boundary and therefore cannot
 153 predict how the channel's geometry might be altered by melting.

154 The hydraulic diameter, D_H , measures the dominant length-scale in the flow problem, tending to the
 155 smaller semi-axis, a or b , in the limit of large or small aspect ratio, respectively. The area of an ellipse has
 156 a simple expression, $A = \pi ab = \pi \xi a^2$, but its perimeter is given by

$$P = 4aE[1 - \xi^2], \quad (13)$$

157 where E is the complete elliptic integral of the second kind, $E[1 - \xi^2] \equiv \int_0^{\pi/2} \sqrt{1 - (1 - \xi^2) \sin^2 \theta} d\theta$. The
 158 hydraulic diameter is therefore given by

$$D_H = \frac{\pi \xi a}{E[1 - \xi^2]}. \quad (14)$$

159 This is the characteristic length scale used to define a Reynolds number for the flow in the elliptical conduit,

$$\text{Re} = \frac{\rho_w D_H U}{\eta_w}, \quad (15)$$

160 which we will use later to determine whether the flow through the channels is laminar or turbulent.

161 Temperature Fields

162 The water's viscosity results in the dissipation of energy, releasing heat. The flow profile determines where
 163 this heat is produced and subsequently where melting occurs. The gradient of the temperature field along
 164 the boundary sets the heat flux into the boundary and hence determines how much melting occurs. Outside
 165 the channel and on the boundary, the ice is assumed to be at the ice's melting temperature,

$$T = T_m \quad \text{on } \partial\Omega. \quad (16)$$

166 This provides the boundary condition for the temperature profile.

167 Laminar

168 For steady laminar flow of an incompressible fluid of constant thermal conductivity, k_T , heat conduction
 169 balances the heat generated by viscous dissipation (Landau and Lifshitz, 1987), so that

$$-k_T \nabla^2 T = \eta_w \left[\left(\frac{\partial u}{\partial y} \right)^2 + \left(\frac{\partial u}{\partial z} \right)^2 \right]. \quad (17)$$

170 We non-dimensionalise using the same scalings as in the flow problem, $y \sim a$, $z \sim b$, $u \sim u_{av} = q/A$, and
 171 scaling the temperature field, T by

$$T_0 = \frac{\eta_w u_{av}^2}{k_T}, \quad (18)$$

172 such that $T = T_m + T_0 \tilde{T}$. Hence, the heat equation (17), becomes

$$\xi^2 \frac{\partial^2 \tilde{T}}{\partial \tilde{y}^2} + \frac{\partial^2 \tilde{T}}{\partial \tilde{z}^2} = - \left[\xi^2 \left(\frac{\partial \tilde{u}}{\partial \tilde{y}} \right)^2 + \left(\frac{\partial \tilde{u}}{\partial \tilde{z}} \right)^2 \right]. \quad (19)$$

173 The known solution to \tilde{u} , (8), can be substituted into this equation to obtain

$$\nabla_{\xi}^2 \tilde{T} = -16(\xi^2 \tilde{y}^2 + \tilde{z}^2) \quad \text{in } \Omega, \quad (20)$$

$$\tilde{T} = 0 \quad \text{on } \partial\Omega. \quad (21)$$

174 Note that the above equation depends only on the aspect ratio ξ . We can solve for the temperature field
175 using a quartic ansatz,

$$\tilde{T} = (\tilde{y}^2 + \tilde{z}^2 - 1) (A\tilde{y}^2 + B\tilde{z}^2 + C), \quad (22)$$

176 that meets the boundary condition, and mirrors the symmetry of the problem. The unknown coefficients
177 are found by substituting into (20) and matching coefficients,

$$A = \frac{4(1 - 6\xi^2 - \xi^4)}{3(1 + 6\xi^2 + \xi^4)}, \quad (23)$$

$$B = -\frac{4(1 + 6\xi^2 - \xi^4)}{3(1 + 6\xi^2 + \xi^4)}, \quad (24)$$

$$C = -\frac{4(1 + 4\xi^2 + \xi^4)}{3(1 + 6\xi^2 + \xi^4)}. \quad (25)$$

178 The resulting rescaled solution for the temperature field for an ellipse where $\xi = 1/2$ is shown in Fig. (2c).
179 In order for the no-slip boundary condition to be met in the laminar flow problem, more shear is required
180 along the shorter semi-axis. This increased shear leads to more heat production, and hence to more melting
181 along this shorter axis, driving evolution of the ellipse towards $\xi = 1$.

182 *Turbulent*

183 In the turbulent limit we expect a turbulent well-mixed and thermally uniform interior surrounded by a
184 thin laminar boundary layer, which has the same depth, δ , everywhere (Schlichting and Gersten, 2017), see
185 Fig. (2b). We follow the Reynolds analogy by assuming that in this turbulent limit, heat and momentum
186 are mixed by the same mechanisms, with the Prandtl number approaching unity, and hence the thermal
187 and velocity boundary layer thicknesses are the same (Reynolds, 1874).

188 We do not attempt to resolve the averaged temperature profile in an elliptical channel but argue that
189 for a constant thickness boundary layer, with a temperature difference ΔT across the layer, the heat flux
190 into the ice, given by $\mathbf{F}_H \simeq \hat{\mathbf{n}} k_T \frac{\Delta T}{\delta}$, where $\hat{\mathbf{n}}$ is unit normal to the surface, must be uniform along the

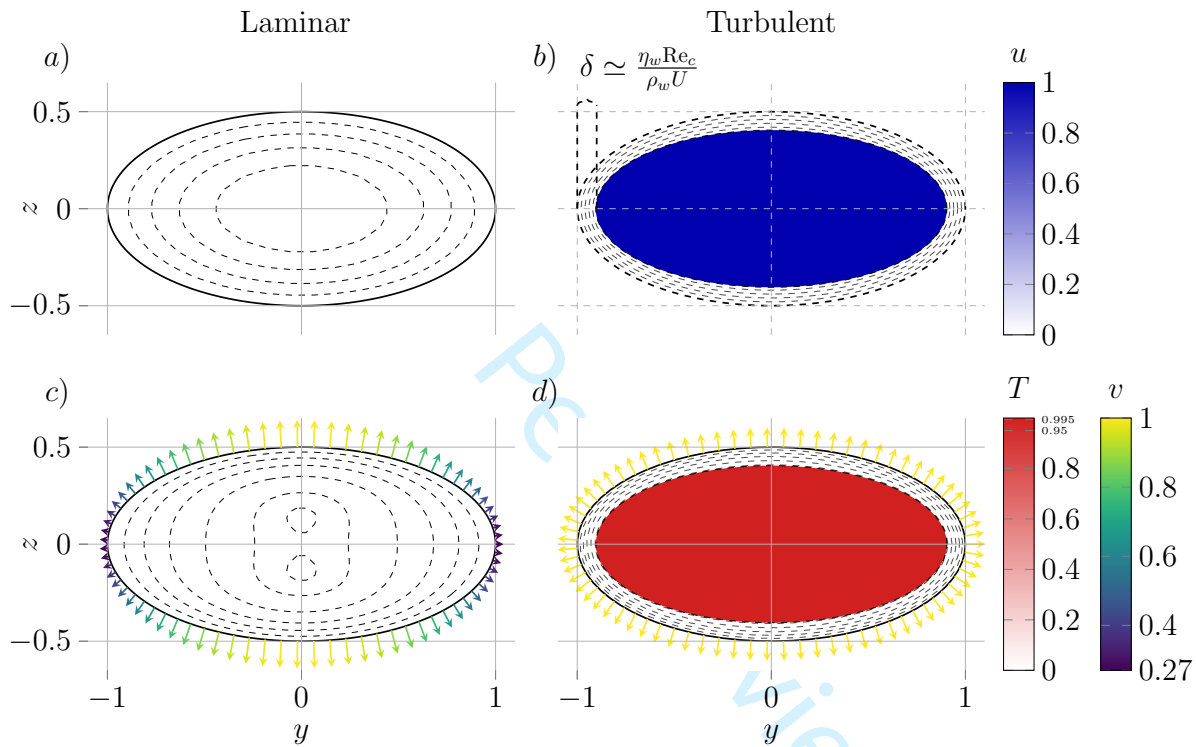


Fig. 2. Flow and temperature profiles for laminar and turbulent flows through an ellipse with aspect ratio $\xi = 1/2$: Velocity profile for laminar (a) and turbulent (b) flows are normalised to a maximal value of one. The turbulent boundary layer thickness, δ , is also labelled. The normalised temperature profiles for laminar (c) and turbulent (d) flow include scaled and coloured arrows representing heat flux into the boundary. All contours match with the labels on the colour bar.

191 boundary, see Fig. (2d).

192 Melting

193 The laminar and turbulent temperature profiles can now be used to calculate both the amount of melt
 194 and how the melt rate at the ice-water interface varies spatially. In the laminar case, where we have a
 195 spatially-resolved temperature profile, we use the temperature gradient in the fluid to find the melt on the
 196 boundary. In the turbulent case, we consider the dissipation of potential energy in the flow, to find the
 197 spatially uniform melt rate. In both the laminar and turbulent melting cases, we expect a change in both
 198 the cross-sectional area and in the aspect ratio of the channel.

199 Laminar

200 The heat flux into the boundary is given by

$$\mathbf{F}_H = -k_T \nabla T, \quad (26)$$

201 where T is the temperature of the water at the boundary. Fig. (2c) shows a scaled variable heat flux into
 202 the boundary for an aspect ratio of $\xi = 1/2$.

203 The heat flux normal to the boundary governs the rate of local melt-back of a section of the boundary,

$$\hat{\mathbf{n}} \cdot \mathbf{F}_H = -k_T \hat{\mathbf{n}} \cdot \nabla T = \rho_i L v_l, \quad (27)$$

204 where ρ_i is the density of the ice, L is the specific latent heat of fusion and v_l is the normal speed of the
 205 boundary in the absence of creep closure. We scale equation (27) as before, such that $y \sim a$, $z \sim b$ and
 206 $T \sim T_0 = \eta_w u_{av}^2 / k_T$, and define the non-dimensional boundary velocity $\tilde{m}_l = v_l / M_l$, where

$$M_l = \frac{\eta_w u_{av}^2}{\rho_i L a}. \quad (28)$$

207 In this scaling the boundary is again mapped to the unit circle, $\tilde{y}^2 + \tilde{z}^2 = 1$, and $\hat{\mathbf{n}} \cdot \tilde{\nabla} \tilde{T}$ is defined, such that

$$\tilde{m}_l = -\frac{\xi^2 \tilde{y} \frac{\partial \tilde{T}}{\partial \tilde{y}} + \tilde{z} \frac{\partial \tilde{T}}{\partial \tilde{z}}}{\xi \sqrt{\xi^2 \tilde{y}^2 + \tilde{z}^2}}. \quad (29)$$

208 Using the temperature field ansatz this becomes

$$\tilde{m}_l(\tilde{y}, \tilde{z}) = -\frac{2[2A\xi^2\tilde{y}^4 + (A+B)(\xi^2+1)\tilde{y}^2\tilde{z}^2 + 2Bz^4 + \xi^2(C-A)\tilde{y}^2 + (C-B)\tilde{z}^2]}{\xi\sqrt{\xi^2\tilde{y}^2 + \tilde{z}^2}}. \quad (30)$$

209 We proceed by assuming that the channel always remains elliptical. The validity of this approximation
 210 is discussed in the appendix. If the cross-section remains elliptical we can describe it using only the
 211 changing lengths of the semi-axes. Therefore, \tilde{m}_l , the melt rate along the entire boundary is only needed at
 212 $(\tilde{y}, \tilde{z}) = (1, 0)$ and $(0, 1)$, denoted \tilde{m}_l^a and \tilde{m}_l^b respectively. This reduces the algebra significantly, and we
 213 find that

$$\tilde{m}_l^a = \frac{16\xi^2}{3} \left(\frac{5 + \xi^2}{1 + 6\xi^2 + \xi^4} \right), \quad (31)$$

$$\tilde{m}_l^b = \frac{16}{3\xi} \left(\frac{5\xi^2 + 1}{1 + 6\xi^2 + \xi^4} \right), \quad (32)$$

214 which we plot in Fig. (3). Note that due to the scaling

$$\frac{d\tilde{a}}{d\tilde{t}} = \tilde{m}_l^a, \quad (33)$$

$$\frac{d\tilde{b}}{d\tilde{t}} = \frac{1}{\xi}\tilde{m}_l^b, \quad (34)$$

215 we have in dimensional form

$$\frac{da}{dt} = M_l\tilde{m}_l^a = \frac{\eta_w q^2}{\pi^2 \xi^2 a^5 \rho_i L} \tilde{m}_l^a, \quad (35)$$

$$\frac{db}{dt} = M_l\tilde{m}_l^b = \frac{\eta_w q^2}{\pi^2 \xi^2 a^5 \rho_i L} \tilde{m}_l^b. \quad (36)$$

216 where we have introduced the non-dimensional melt-back time $\tilde{t} = t/t_0$, where the timescale

$$t_0 = \frac{a}{M_l}. \quad (37)$$

217 To simplify future analyses, the ξ dependent scaling is removed by introducing V_l and \tilde{v}_l , where $V_l = M_l\xi^2$

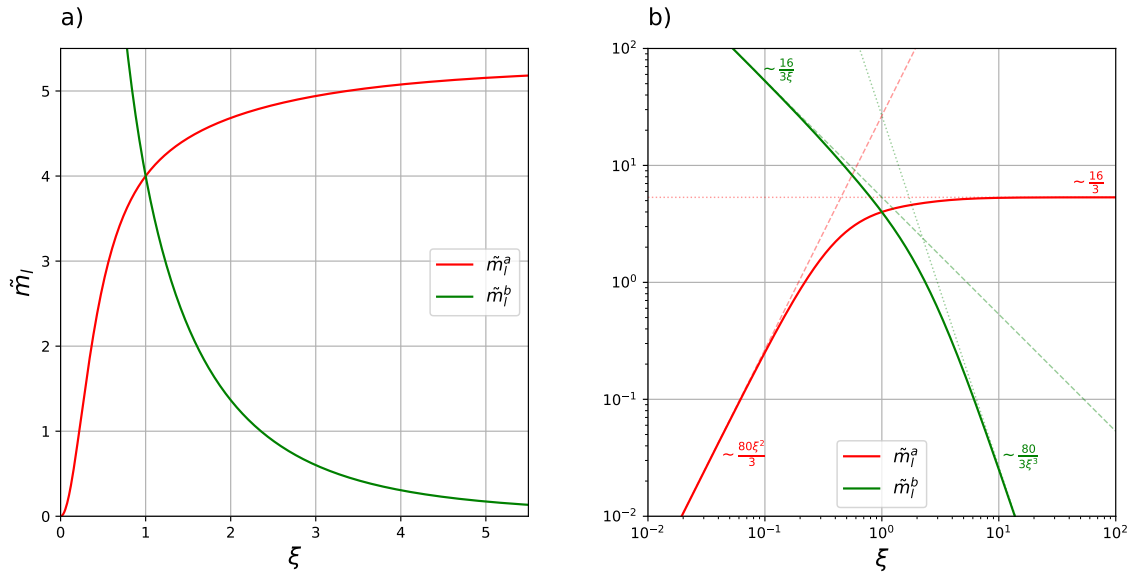


Fig. 3. Dimensionless laminar melt rates \tilde{m}_l along the semi-axes \tilde{a} (red) and \tilde{b} (green) versus aspect ratio ξ . (a) Linear scale highlighting the regime where $\xi \sim O(1)$. (b) Log-log scale showing the convergence of the analytical expressions to their leading-order asymptotic limits (dashed) as $\xi \rightarrow 0$ and $\xi \rightarrow \infty$. Labels indicate the specific power-law scaling for each limit.

218 and $\tilde{v}_l = \tilde{m}_l/\xi^2$, such that

$$\frac{da}{dt} = V_l \tilde{v}_l^a = \frac{\eta_w q^2}{\pi^2 a^5 \rho_i L} \tilde{v}_l^a, \quad (38)$$

$$\frac{db}{dt} = V_l \tilde{v}_l^b = \frac{\eta_w q^2}{\pi^2 a^5 \rho_i L} \tilde{v}_l^b. \quad (39)$$

219 Note that by the symmetry of the problem the equations are equivalent under the exchange $a \rightleftharpoons b$ and
 220 $\xi \rightleftharpoons 1/\xi$.

221 *Turbulent*

222 In the limit of turbulent flow, $\text{Re} \rightarrow \infty$, we expect a well mixed interior with a uniform temperature. As
 223 discussed earlier, we assume a boundary layer with a uniform thickness and therefore a spatially uniform
 224 melt rate along the boundary. We conclude that the melt rates of the semi-axes must be equal, defining
 225 $v_t = \frac{da}{dt} = \frac{db}{dt}$ as the turbulent melt rate.

226 We assume that the total heat flux in the turbulent limit, without resolving the flow profile, by assuming
 227 that the fluid's power loss, qG , is transformed to heat that is completely converted into melting the boundary

228 of the ellipse.

229 We note that as the water moves to a lower pressure, energy is required to maintain the water at the
 230 melting temperature due to the change in pressure-melting point. Röthlisberger (1972) estimates this to be
 231 about a third of the total available energy. Here, and in the laminar flow problem, as in Walder and Fowler
 232 (1994), we ignore this effect for algebraic convenience and expect it to make only a quantitative but not
 233 qualitative difference to our results.

234 Additionally, because we assume that the ice is everywhere at its melting temperature, the heat entering
 235 the boundary causes only melt (no change in sensible heat). The channel wall melting power, qG , therefore,
 236 alters the channel's area,

$$qG = \rho_i L \frac{dA}{dt}, \quad (40)$$

237 We use the cross-sectional area πab , to rearrange and apply the chain rule,

$$\frac{qG}{\rho_i L} = \frac{dA}{dt} = \pi \left(\frac{da}{dt} b + a \frac{db}{dt} \right) = \pi(a + b)v_t, \quad (41)$$

238 from which we can find an expression for the melt rate

$$\frac{da}{dt} = \frac{db}{dt} = v_t = \frac{qG}{\rho_i L \pi a(\xi + 1)}. \quad (42)$$

239 Using the Darcy-Weisbach equation, (12), we can replace the pressure gradient, G , with an expression
 240 involving the imposed flux,

$$v_t = \frac{f_D \rho_w q^3}{2\pi^4 a^6 \rho_i L} \frac{E[1 - \xi^2]}{\xi^3(\xi + 1)} \equiv \frac{f_D \rho_w q^3}{2\pi^4 a^6 \rho_i L} \tilde{v}_t(\xi), \quad (43)$$

241 where we have introduced a dimensionless turbulent melt rate $\tilde{v}_t(\xi)$ that depends only on the aspect ratio.
 242 Note, this dependence on ξ is predominantly due to the change in resistance to flow due to the geometry
 243 of the channel. For example, for fixed semi-axis a and fixed flux q , we expect a small ξ to result in a
 244 thin (eccentric) channel. Maintaining a constant flux through this narrower channel requires an increase
 245 in the pressure gradient, and hence results in an increase in the uniform melt rate $\sim qG$. Since the melt
 246 rate is equal in all directions in the turbulent limit, we expect only a weak tendency to melt into circular
 247 cross-sections.

248 *Hybridised Laminar–Turbulent Melt Scheme*

249 In both the laminar and turbulent limits, we have considered constant flux conditions, without considering
 250 whether the resulting flow is indeed turbulent. Since a given constant flux will result in a range of Reynolds
 251 numbers for a range of channel sizes and shapes (e.g. if a fixed flux results in slow, laminar flow in a large
 252 channel we expect the same flux to result in fast, turbulent flow for smaller channel sizes), we propose a
 253 simple patching approach between regimes using a sigmoid function. Considering only the laminar v_l^a, v_l^b
 254 and turbulent v_t melting terms, we propose that the effective melt rate can be parametrised in terms of the
 255 Reynolds number as

$$\frac{da}{dt} = \frac{v_l^a - v_t}{1 + e^{k(\text{Re} - \text{Re}_c)}} + v_t, \quad (44)$$

$$\frac{db}{dt} = \frac{v_l^b - v_t}{1 + e^{k(\text{Re} - \text{Re}_c)}} + v_t. \quad (45)$$

256 Here we have introduced, $k > 0$ which sets the range of Reynolds numbers over which the melting transitions
 257 from laminar melt to turbulent melt and Re_c , the critical Reynolds number where this transition, from
 258 laminar melting to turbulent melting, is expected to occur. We do not attempt to resolve the intermediate
 259 or critical flow regime. Instead, the sigmoidal formulation provides a simple method to smoothly transition
 260 between the two melt regimes, ensuring that the appropriate behaviour in the extremal limits of Re are
 261 recovered, and providing a transition width, governed by k , over which the flow and temperature field are
 262 approximately continuous. The choice of k , as will be discussed later, does not qualitatively affect the
 263 resulting stable points or dynamics.

264 In the intermediate regime, we might expect to see a boundary layer that depends on the local curvature
 265 and hence aspect ratio, resulting in some variability in the melt rate across the ice-water interface. This
 266 variable melt rate is potentially captured to some extent by our patching approach, but a full direct
 267 numerical simulation of the turbulent flow and thermal fields would be required to confirm this. We note
 268 that a model that could, for example, incorporate pockets of laminar flow near the higher curvature tips of
 269 the ellipses would likely result in greater forcing towards circular cross-sections for comparatively higher
 270 bulk-flow Reynolds numbers. Nevertheless, the hybridised scheme presented here captures the essential
 271 behaviour of the system simply, and is likely to be at least qualitatively correct.

272 Viscous Collapse of the Surrounding Ice

273 Regardless of the Reynolds number of the flow inside the channel, the surrounding ice flows and collapses
 274 as a very viscous fluid. Dallaston and Hewitt (2014) found that the elliptical cross-section was stable for
 275 channels experiencing only creep closure and where the rheology of the ice was taken to be Newtonian.
 276 Their solution to the Stokes flow problem gives the evolution equations

$$\frac{da}{dt} = -\frac{1}{2} \frac{N}{\eta_i} b, \quad (46)$$

$$\frac{db}{dt} = -\frac{1}{2} \frac{N}{\eta_i} a, \quad (47)$$

277 with effective pressure N , as defined in the introduction, and viscosity of the ice η_i . These simultaneous
 278 equations show that without melt channels with eccentric ellipses are driven strongly towards higher
 279 eccentricities, collapsing into a line in finite time.

280 RESULTS

281 We now combine the model melting term with the viscous collapse in the ice. We have described the flow
 282 through the channel in both the laminar and turbulent limits and used these to calculate a melt rate of the
 283 ice-water boundary. The melt rates for laminar and turbulent melt have been combined into one hybrid
 284 laminar–turbulent melt scheme that depends on the Reynolds number of the flow. The fully dimensional
 285 hybrid melt equation is combined with the viscous creep to give

$$\frac{da}{dt} = -\frac{1}{2} \frac{N}{\eta_i} b + \frac{V_l \tilde{v}_l^a - V_t \tilde{v}_t}{1 + e^{k(\text{Re} - \text{Re}_c)}} + V_t \tilde{v}_t, \quad (48)$$

$$\frac{db}{dt} = -\frac{1}{2} \frac{N}{\eta_i} a + \frac{V_l \tilde{v}_l^b - V_t \tilde{v}_t}{1 + e^{k(\text{Re} - \text{Re}_c)}} + V_t \tilde{v}_t, \quad (49)$$

286 where we have split the laminar and turbulent melt rates into their dimensional (V) and dimensionless (\tilde{v})
 287 parts. Note that above $\tilde{v} = \tilde{v}(\xi)$ only. To proceed, we non-dimensionalise once again. Time is now scaled to
 288 the characteristic timescale of creep closure, $t = t_0 \tilde{t}$ where $t_0 = \eta_i/N$. We choose a time-independent length
 289 scale dependent on the only fixed natural scale of the problem

$$\ell^6 = \frac{\eta_w q^2}{\pi^2 \rho_i L} \frac{\eta_i}{N}, \quad (50)$$

290 so that now $a = \ell\tilde{a}$, $b = \ell\tilde{b}$. Note that this ℓ is approximately the size of a channel for which laminar melting
 291 and viscous collapse are balanced, since $\ell = V_l t_0$ and $V_l = \frac{\eta_w q^2}{\pi^2 \tilde{a}^3 \rho_i L}$ is the melt-back velocity of the boundary
 292 used in the scaling for equation (39). With these rescalings we now have

$$\frac{d\tilde{a}}{d\tilde{t}} = -\frac{\tilde{b}}{2} + \frac{1}{\tilde{a}^5} \left(\frac{\tilde{v}_l^a - \frac{f_D q \rho_w}{2\pi^2 \eta_w \ell \tilde{a}} \tilde{v}_t}{1 + e^{k(\text{Re} - \text{Re}_c)}} + \frac{f_D q \rho_w}{2\pi^2 \eta_w \ell \tilde{a}} \tilde{v}_t \right), \quad (51)$$

$$\frac{d\tilde{b}}{d\tilde{t}} = -\frac{\tilde{a}}{2} + \frac{1}{\tilde{a}^5} \left(\frac{\tilde{v}_l^b - \frac{f_D q \rho_w}{2\pi^2 \eta_w \ell \tilde{a}} \tilde{v}_t}{1 + e^{k(\text{Re} - \text{Re}_c)}} + \frac{f_D q \rho_w}{2\pi^2 \eta_w \ell \tilde{a}} \tilde{v}_t \right). \quad (52)$$

293 The Reynolds number, as previously defined in (15), depends on both a and b , through the hydraulic
 294 diameter D_H and U . Here, we assume that the average flow speed q/A is approximately equal to the bulk
 295 flow speed U in turbulent flow. Rewriting directly in terms of the flux and the geometry of the channel we
 296 have

$$\text{Re} = \frac{\rho_w q}{\eta_w a E [1 - \xi^2]}. \quad (53)$$

297 Replacing a by its non-dimensional version we therefore write

$$\text{Re} = \frac{\rho_w q}{\eta_w \ell \tilde{a} E [1 - \xi^2]} \equiv \frac{\mathcal{Q}}{\tilde{a} E [1 - \xi^2]}, \quad (54)$$

298 where we have introduced $\mathcal{Q} = \rho_w q / \eta_w \ell$, a dimensionless number acting as a proxy for the Reynolds number
 299 which is constant in time despite an evolving size and aspect ratio. Note that $\mathcal{Q} \sim q^{2/3}$ since $\ell \sim q^{1/3}$ from
 300 (50). For otherwise fixed parameters (η_w , η_i , ρ_w , ρ_i , L , and N), \mathcal{Q} is therefore related to the imposed flux,
 301 and we name it the dimensionless flux number. From (54) we also note that \mathcal{Q} is equal to the Reynolds
 302 number for a circular channel with a non-dimensional radius $\tilde{a} = 2/\pi$. For a larger circular channel with
 303 the same dimensionless flux number, we would expect a lower Reynolds number in the flow for the same
 304 flux number \mathcal{Q} . Non-circular cross-sections will again have an altered Reynolds number.

305 This scaling simplifies the simultaneous equations to

$$\frac{d\tilde{a}}{d\tilde{t}} = -\frac{\tilde{b}}{2} + \frac{1}{\tilde{a}^5} \left(\frac{\tilde{v}_l^a - \frac{1}{\tilde{a}} \frac{f_D \mathcal{Q}}{2\pi^2} \tilde{v}_t}{1 + e^{k\left(\frac{\mathcal{Q}}{\tilde{a} E [1 - \xi^2]} - \text{Re}_c\right)}} + \frac{1}{\tilde{a}} \frac{f_D \mathcal{Q}}{2\pi^2} \tilde{v}_t \right), \quad (55)$$

$$\frac{d\tilde{b}}{d\tilde{t}} = -\frac{\tilde{a}}{2} + \frac{1}{\tilde{a}^5} \left(\frac{\tilde{v}_l^b - \frac{1}{\tilde{a}} \frac{f_D \mathcal{Q}}{2\pi^2} \tilde{v}_t}{1 + e^{k\left(\frac{\mathcal{Q}}{\tilde{a} E [1 - \xi^2]} - \text{Re}_c\right)}} + \frac{1}{\tilde{a}} \frac{f_D \mathcal{Q}}{2\pi^2} \tilde{v}_t \right), \quad (56)$$

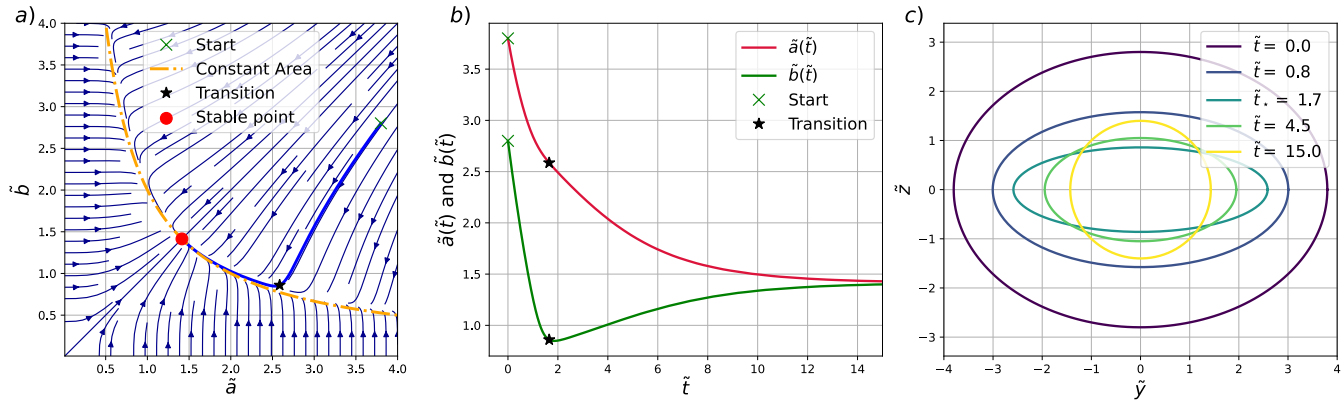


Fig. 4. The phase field plot (a) with scaled semi-axes shows a trajectory (thick blue line) of a channel dominated by laminar flow initiated with a large area. The channel decreases in size, reaching the “transition”, before travelling close to the contour of fixed area to the stable point. The trajectories of the semi-axes in (a) are shown independently in (b), and snapshots of the channel cross-sections (c) show a clear migration towards a circular cross-section.

306 where

$$\tilde{v}_l^a = \frac{16}{3} \left(\frac{5 + \xi^2}{1 + 6\xi^2 + \xi^4} \right), \quad (57)$$

$$\tilde{v}_l^b = \frac{16}{3\xi^3} \left(\frac{5\xi^2 + 1}{1 + 6\xi^2 + \xi^4} \right), \quad (58)$$

$$\tilde{v}_t = \frac{E[1 - \xi^2]}{\xi^3(\xi + 1)}, \quad (59)$$

$$\xi = \frac{\tilde{b}}{\tilde{a}}. \quad (60)$$

307 We are left with a non-dimensionalised system of coupled differential equations with four non-dimensional
 308 parameters: the friction factor f_D , the sharpness k and position Re_c of the transition between laminar and
 309 turbulent melt and the dimensionless flux number \mathcal{Q} . We assume that k , Re_c and f_D are physical constants,
 310 leaving only \mathcal{Q} as a non-dimensional variable to parametrise the meltwater input.

311 To analyse this system, we will briefly consider the limits of laminar and turbulent flow before considering
 312 the full hybrid laminar–turbulent model.

313 *Laminar Evolution*

314 In the limit as $\mathcal{Q} \rightarrow 0$ (low flux and low Reynolds number even for the smallest channels) we recover a
 315 combination of laminar melt with viscous collapse,

$$\frac{d\tilde{a}}{d\tilde{t}} = -\frac{\tilde{b}}{2} + \frac{16}{3\tilde{a}^5} \left(\frac{5 + \xi^2}{1 + 6\xi^2 + \xi^4} \right), \quad (61)$$

$$\frac{d\tilde{b}}{d\tilde{t}} = -\frac{\tilde{a}}{2} + \frac{16}{3\tilde{a}^5\xi^3} \left(\frac{5\xi^2 + 1}{1 + 6\xi^2 + \xi^4} \right). \quad (62)$$

316 The evolution of the elliptical channels can be visualised in this limit using a phase field plot (Fig. 4). We
 317 see the dynamics approximately collapse rapidly towards a contour of fixed area. Once a channel reaches
 318 this area, it will slowly migrate towards a circular cross-section. This is the global stable point for the
 319 system, and any initial channel size or shape will evolve towards this state. By symmetry, the stable point
 320 occurs at a circular cross-section ($\xi = 1$) when $\dot{\tilde{a}} = \dot{\tilde{b}} = 0$, for which

$$\tilde{a} = \tilde{b} = \sqrt{2}. \quad (63)$$

321 In the vicinity of the equilibrium point we expect the behaviour to be well described by a first order
 322 expansion of the simultaneous equations,

$$\begin{pmatrix} \dot{\tilde{a}} \\ \dot{\tilde{b}} \end{pmatrix} \approx \begin{pmatrix} \frac{\partial \dot{\tilde{a}}}{\partial \tilde{a}} & \frac{\partial \dot{\tilde{a}}}{\partial \tilde{b}} \\ \frac{\partial \dot{\tilde{b}}}{\partial \tilde{a}} & \frac{\partial \dot{\tilde{b}}}{\partial \tilde{b}} \end{pmatrix} \begin{pmatrix} \delta\tilde{a} \\ \delta\tilde{b} \end{pmatrix}, \quad (64)$$

323 where the Jacobian matrix expresses the first order Taylor expansion. For this system of equations we find
 324 the eigenvalues and eigenvectors to be

$$e_1 = -\frac{1}{3}, \quad \mathbf{e}_1 = \frac{1}{\sqrt{2}} \begin{pmatrix} 1 \\ -1 \end{pmatrix}, \quad (65)$$

$$e_2 = -3, \quad \mathbf{e}_2 = \frac{1}{\sqrt{2}} \begin{pmatrix} 1 \\ 1 \end{pmatrix}. \quad (66)$$

326 Since both eigenvalues are negative we conclude this point is stable. The $(1, -1)$ direction is tangential to a
 327 contour of fixed area that passes through the stable point given by $\tilde{b} = 2/\tilde{a}$. The discrepancy in the sizes of

328 the eigenvalues indicates that the evolution along this contour is significantly slower than the evolution
 329 towards it, as can be seen in the middle plot of Fig. (4).

330 We have found that the strong spatial variation in the melt rate along the boundary due to laminar flow
 331 dominates over the viscous collapse term and hence channels evolve towards circular cross-sections with
 332 $\tilde{a} = \sqrt{2}$. Re-dimensionalising this stable point lets us estimate the sizes of channels that are opened by
 333 melting in purely laminar flow. We find that

$$a = b = \sqrt{2} \left(\frac{\eta_w q^2 \eta_i}{\pi^2 \rho_i L N} \right)^{1/6} \sim q^{1/3}. \quad (67)$$

334 However, for the flow to be laminar the Reynolds number must be smaller than the critical value which we
 335 assume to be of the order $\text{Re}_c \simeq 10^3$. In terms of q and a , this is equivalent to

$$q < \frac{\pi \eta_w \text{Re}_c}{\rho_i} a, \quad (68)$$

336 which places a restriction on the maximum size of these laminar channels,

$$a < \left(\frac{8 \eta_w^3 \eta_i}{\rho_w^2 \rho_i L N} \right)^{1/4} \sqrt{\text{Re}_c} \simeq 1 \text{ cm}, \quad (69)$$

337 with a maximal flow rate of $q \sim 10^{-5} \text{ m}^3 \text{ s}^{-1}$. Here we have used rough estimates: $\eta_w \sim 10^{-3} \text{ Pa s}$,
 338 $\eta_i \sim 10^{15} \text{ Pa s}$, $\rho_w \sim \rho_i \sim 10^3 \text{ kg m}^{-3}$, $L \sim 10^5 \text{ J kg}^{-1}$ and $N \sim 10^6 \text{ Pa}$. Although channel cross-sections are
 339 frequently observed at larger scales 0.1 – 100 m (Cuffey and Paterson, 2010; Kamintzis and others, 2023),
 340 basal conduits at the interface between the ice and bedrock have, however, been observed with heights of
 341 0.01 m (Hooke and others, 1990). Suggesting that these laminar dynamics may be especially relevant in
 342 linked-cavity systems or canals. The apparent scarcity of observations of channels of this scale is potentially
 343 attributable to resolution limits of current techniques. Furthermore, as conduits grow and their capacity
 344 increases, they must inevitably transition to hybrid or turbulent flow to achieve larger-scale geometries
 345 characteristic of fully developed arborescent networks. This result suggests an important threshold for the
 346 transition from incipient, laminar-dominated localization to turbulent channelisation.

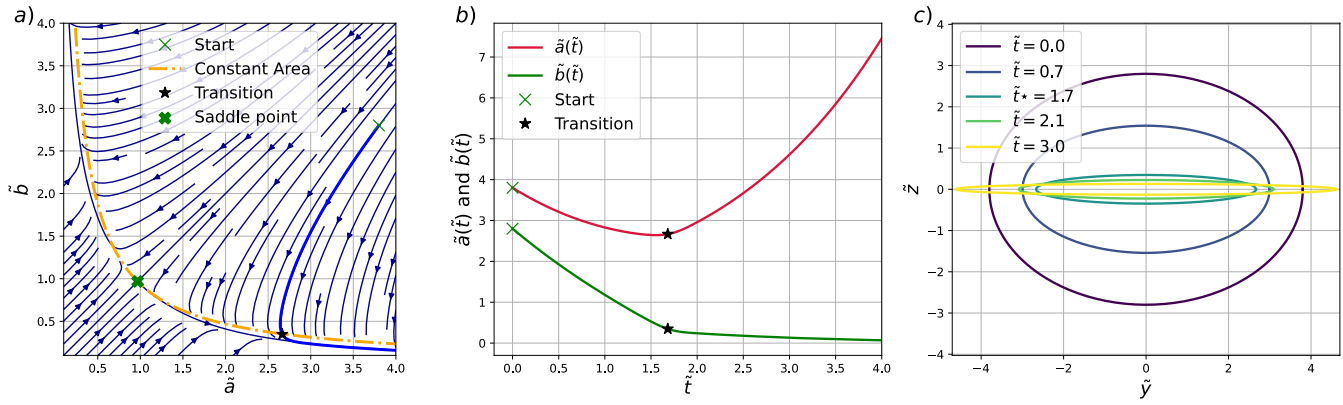


Fig. 5. The phase field plot (a) with scaled semi-axes shows a trajectory (thick blue line) of a channel dominated by turbulent flow initiated with a large area. The channel decreases in size, reaching the “transition”, before travelling close to the contour of fixed area away from the saddle point. The trajectories of the semi-axes in (a) are shown independently in (b), and snapshots of the channel cross-sections (c) show migration towards a continually narrowing channel.

347 *Turbulent Evolution*

348 In the $Q \rightarrow \infty$ limit, we recover a model of purely turbulent melting together with the viscous collapse of
 349 the ice,

$$\frac{d\tilde{a}}{d\tilde{t}} = -\frac{\tilde{b}}{2} + \frac{1}{\tilde{a}^6} \frac{f_D Q}{2\pi^2} \frac{E[1-\xi^2]}{\xi^3(\xi+1)}, \quad (70)$$

$$\frac{d\tilde{b}}{d\tilde{t}} = -\frac{\tilde{a}}{2} + \frac{1}{\tilde{a}^6} \frac{f_D Q}{2\pi^2} \frac{E[1-\xi^2]}{\xi^3(\xi+1)}. \quad (71)$$

350 A phase field plot in Fig. (5) shows that there exists a single stationary point for the combined system
 351 when $\xi = 1$, $\tilde{a} = \tilde{b} = \left(\frac{f_D Q}{4\pi}\right)^{1/7}$. Using the same Jacobian approach, we find that this point is stable in the
 352 $(1, 1)$ direction with an eigenvalue of -7 . However, an eigenvalue of 1 in the $(1, -1)$ direction implies that
 353 these turbulent channels are unstable. The saddle-point when re-dimensionalised is of size

$$a_{\text{saddle}} = \left(\frac{f_D \rho_w q^3 \eta_i}{4\pi^3 \rho_i L N} \right)^{1/7}, \quad (72)$$

354 so that with $f_D \simeq 10^{-3}$ in the turbulent limit we find that

$$a_{\text{saddle}} \sim \frac{q^{3/7}}{m^{2/7} s^{-3/7}}. \quad (73)$$

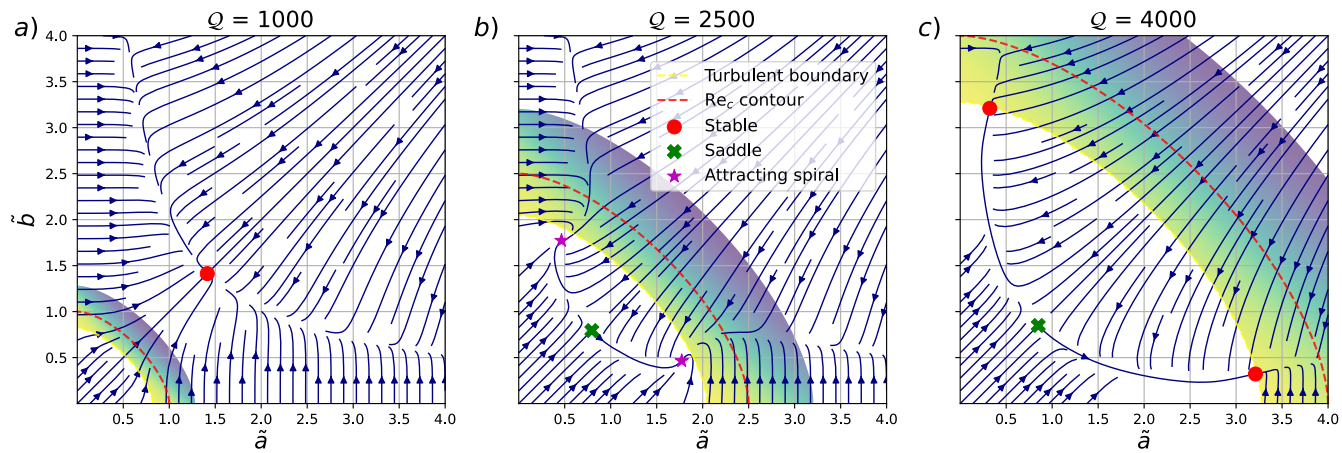


Fig. 6. The dynamics of a channel with hybridised flow and viscous closure of ice is shown using phase field plots for increasing Q . The coloured band marks the transition region from turbulent (bottom left) to laminar (top right) flow. The turbulent and laminar boundaries indicate where 90% of the melting is from the turbulent or laminar melt term, respectively. In (a) the \tilde{a}, \tilde{b} domain is dominated by laminar melting for low $Q = 1000$. In (b) for increasing $Q = 2500$ stable, spiral attractors in the turbulent region with eccentric cross-sections are found. A further increase in $Q = 4000$, shown in (c), results in the expected saddle point as before but now with new stable points with higher eccentricities. The general parameters used here are $Re_c = 10^3$, $k = 10^{-2}$ and $f_D = 10^{-3}$.

355 A volume flux of $1 \text{ m}^3 \text{ s}^{-1}$ therefore results in a 1 m wide (unstable) channel for the same parameter values
 356 used in the laminar case.

357 We note that an analysis, such as R othlisberger's, that does not consider non-circular channels would
 358 mistakenly conclude that a stable state exists for purely turbulent flow. By allowing the eccentricity to
 359 evolve, we find the weak tendency for turbulent melting to evolve towards circular channels is dominated by
 360 the much stronger forcing from the viscous collapse which tends to drive the geometry towards increasing
 361 eccentricities. We therefore suggest that in the turbulent limit, all channels collapse to an infinite or zero
 362 aspect ratio. This aligns with the findings of Dallaston and Hewitt (2014) who noted an instability in
 363 channels with free boundaries under uniform heating. Though ellipses did not form an exact solution,
 364 perturbations of a circular channel demonstrate a comparable instability that drives the system toward
 365 singularity.

366 *Hybrid Laminar–Turbulent Evolution*

367 This continued collapse towards ever narrowing channels in the turbulent case, motivates our introduction of
 368 a hybrid laminar–turbulent melt parametrisation. As the channel thins (increasing eccentricity), we expect

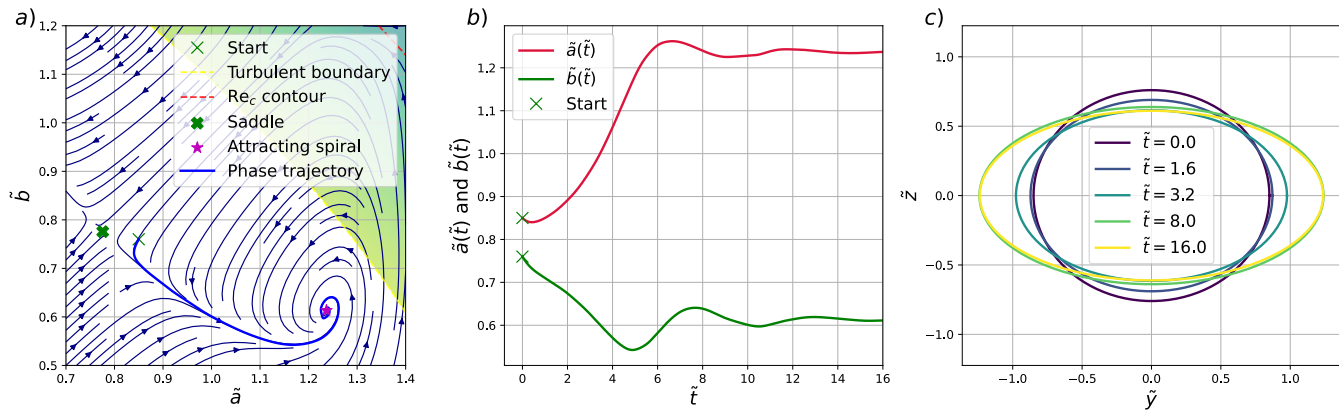


Fig. 7. The dynamics of a channel with hybridised water flow and viscous closure of ice. The phase field plot (a) with scaled semi-axes shows a trajectory (thick blue line) starting near the turbulent saddle point and orbiting a spiral attractor. The trajectories of the scaled semi-axes in (a) are shown independently in (b), and snapshots of the channel cross-sections (c) show settling towards an elliptical cross-section. The parameters used here are $Re_c = 10^3$, $k = 10^{-2}$, $Q = 2000$ and $f_D = 10^{-3}$

369 the flow to eventually become laminar, similar to a Hele-Shaw type flow with near parallel top and bottom
 370 boundaries. As we approach laminar flow, we expect a much stronger forcing towards circular channels,
 371 potentially leading to an intermediate stable configuration with a finite eccentricity channel cross-section.

372 In Fig. (6) we show the phase field plots for the hybridised melting scheme for three increasing values
 373 of Q . The phase field plots for the smallest and largest flux numbers have domains that are dominated
 374 by phase streamlines similar to those found in the laminar and turbulent limits, with the same stationary
 375 points. However, at sufficiently large values of Q , we find new stationary points off the circular ($\xi = 1$) axis.

376 For a fixed flux, this approach provides a continuous projection for the channel cross-section as it evolves
 377 through various values of the Reynolds number. The phase trajectory shown in Fig. (7) shows the behaviour
 378 of one such channel cross-section evolving toward critical Reynolds number flows with higher eccentricities,
 379 until it approaches a new non-circular stable point. Heuristically, we find that channels rapidly converge to
 380 stable cross-sectional areas before evolving toward higher eccentricities, until they become narrow enough for
 381 the transition to laminar flow to begin at which point they stabilise. Alternatively, if the channel begins as
 382 eccentric and laminar it will melt towards a circular cross-section until the flow begins to become turbulent.
 383 Fig. (8) shows the location of the stable channel size with increasing Q .

384 We can approximate these stable cross-sections by finding where the contours of constant area of the
 385 purely turbulent and purely laminar systems, passing through their stationary points, intersect the critical

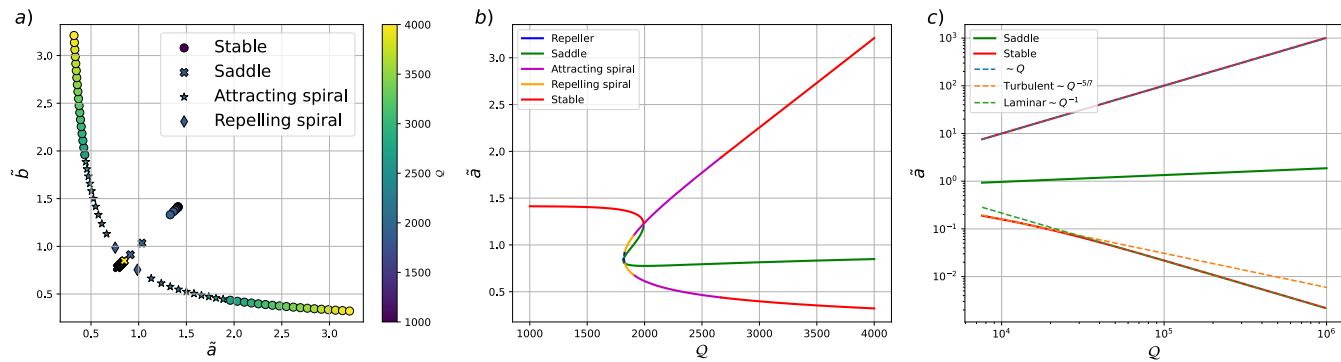


Fig. 8. The variation in the type and position of stationary points as a function of Q : The shapes in (a) show the type of stationary point in phase space with the colour representing Q . We see a clear bifurcation above $Q \sim 2\text{Re}_c$ in (b), where one semi-axis is plotted against Q . The Log-log plot (c) of this bifurcation shows the power-law-like dependence for large Q — as the asymptotic predictions are more accurate for narrow transition regions, $k = 0.5$ was used in this plot. These stationary points were found using a numerical scheme that used multiple initial guesses distributed across the (\tilde{a}, \tilde{b}) domain to sample distinct basins of attraction. Locally, stability was determined by computing the Jacobian numerically via finite differences. The parameters used here are $\text{Re}_c = 10^3$, $k = 10^{-2}$ for (a) and (b) and $k = 0.5$ for (c), and $f_D = 10^{-3}$.

386 Reynolds number contour. This analysis is sensitive to the choice in k . A larger k (~ 0.5) narrows the
 387 transition region, improving the approximation that the stable point lies at the intersection. Additionally, k
 388 affects the minimum value of Q at which a stable elliptical cross-sections exists, though this effect is small
 389 in comparison to the choice in Re_c — bifurcation happens near $Q \sim 2\text{Re}_c$. In the following, we shall assume
 390 a larger value for k , but note that smaller values of k ($\simeq 0.01$) will result in quantitative deviations from
 391 these approximations. An exact treatment of the intersection of the curves results in an equation without a
 392 simple closed-form solution. Instead, here we find approximate solutions, which we hope are more readily
 393 useable in diverse applications. The constant area contours are given by

$$\tilde{b} = \frac{2}{\tilde{a}}, \quad (74)$$

394 for the laminar regime and

$$\tilde{b} = \left(\frac{f_D Q}{4\pi} \right)^{2/7} \frac{1}{\tilde{a}}, \quad (75)$$

395 for the turbulent regime. In the limit of large $Q \gg 1$, we expect highly eccentric solutions with \tilde{b} approaching
 396 zero. Near here, we can approximate the Re_c contour as vertical, with $\tilde{a} = Q/\text{Re}_c$. Note that the other

397 stable solution near $\tilde{b} = Q/\text{Re}_c$ is symmetric and can be found under the exchange of \tilde{a} with \tilde{b} . For the root
 398 near $\tilde{a} = Q/\text{Re}_c$, there are intersections for the laminar and turbulent constant areas, given as

$$\tilde{a} = \frac{Q}{\text{Re}_c}, \quad \tilde{b} = 2\frac{\text{Re}_c}{Q}, \quad (76)$$

$$\tilde{a} = \frac{Q}{\text{Re}_c}, \quad \tilde{b} = \left(\frac{f_D}{4\pi}\right)^{2/7} \frac{\text{Re}_c}{Q^{5/7}}, \quad (77)$$

399 respectively. The roots are equal for $Q = 32\sqrt{2}\pi/f_D$. We coarsely assume that the stable point must lie
 400 between these two intersections. These approximate solutions along with the numerical solutions have been
 401 plotted in Fig. (8). We note that the laminar intersection is appropriate above $Q \sim 32\sqrt{2}\pi/f_D$, whilst the
 402 turbulent intersection is most appropriate below this threshold.

403 Up to this point, we have only considered conditions of constant flux. However, it is simple enough
 404 to alter the above calculations to consider a condition of constant pressure gradient. Under a constant
 405 pressure gradient, melt-back grows with the hydraulic diameter of the channel faster than the collapse,
 406 leading to an ever-growing cross-section. Hence, similar to Röhrlisberger (1972), no stable solutions are
 407 found in the laminar, turbulent or hybrid case for conditions of constant pressure gradient.

408 Flux and Pressure Gradients for Stable Cross-Sections

409 In steady state, the balance between the melting power, qG (which is a combination of pressure gradient and
 410 fluid flux), and the effective pressure in the channel N driving its creeping closure results in expressions that
 411 have provided insight into the evolution of a subglacial network. Röhrlisberger (1972) considered turbulent
 412 circular channels and found an inverse relation between the pressure gradient G and flux q . A similar
 413 approach, in the purely turbulent case, where we use the unstable circular cross-section from equation (72)
 414 with the turbulent flow law equation (12) suggests that

$$G = \left(\frac{\pi f_D^2 \rho_i^5 L^5 N^5}{16\eta_i^5 q}\right)^{1/7} \sim N^{5/7} q^{-1/7}. \quad (78)$$

415 In the laminar case, we found the stable circular cross-section with $a \sim N^{-1/6} q^{1/3}$ from (67). The
 416 pressure gradient required for this channel is found, using equation (5) so that $q \sim GA \sim Ga^4$, to scale as

417 $G \sim N^{2/3}q^{-1/3}$, and hence, in full,

$$G = \left(\frac{8\pi\eta_w\rho_i^2L^2N^2}{\eta_i^2q} \right)^{1/3} \sim N^{2/3}q^{-1/3} \quad (79)$$

418 for laminar channels.

419 We note that in both the laminar and turbulent cases a greater flux results in a lower required pressure
 420 gradient. This suggests that larger channels, which transport more water and hence require lower pressure
 421 gradients, will steal the water from neighbouring smaller channels (assuming similar distances to, and
 422 pressures at their termini). R othlisberger (1972) found similar relations, though with slightly different
 423 exponents due to his choice of the Gauckler-Manning-Strickler turbulent flow law, and considered this as
 424 proof that intra- and subglacial water flows in channels with a tendency towards fewer, larger channels.

425 Walder and Fowler (1994) applied the ideas of R othlisberger (1972) to a wider range of subglacial
 426 drainage elements, but instead considered the relationship between the effective pressure and flux, by
 427 assuming that the pressure gradient is imposed only by the glacial surface topography. This results in
 428 equivalent conclusions to those deduced here since, for example (79) predicts that $N \sim q^{1/2}$, suggesting an
 429 increase in flux increases the effective pressure, or equivalently lowers the water pressure, p_w , in the channel,
 430 since $N = p_i - p_w$. Walder and Fowler (1994) found a contrary relation for canals, however, $N \sim q^{-1/n}$,
 431 where n is the exponent in Glen's flow law for ice. Canals, therefore form non-arborescent subglacial systems,
 432 more consistent with a distributed rather than channelised drainage network. Their work also considered
 433 Darcy flow through subglacial till which similarly behaved as a distributed system. Ng (2000) confirmed
 434 the distributed nature of canals by providing a more detailed model that incorporates the mechanics of
 435 sediment transport within these canals, finding $N \sim q^{-\frac{5}{2n}}$.

436 For the hybridised stable non-circular cross-sections we expect flow to evolve to a state near criticality,
 437 where the laminar and turbulent flow laws would not be appropriate to derive a relation between q , G
 438 and N . Instead, we consider the flow-type-independent equation (40) with the numerical results for stable
 439 channel cross-sectional areas given by a and b . Since in a steady state, the melting term must be equal to
 440 the collapse term, da/dt in (40) must be equal to $bN/2\eta_i$, from the dimensional governing equation (48).
 441 This simplifies to

$$G = \frac{\pi\rho_iL}{q} \left(\frac{da}{dt}b + a\frac{db}{dt} \right) = \left(\frac{\pi\rho_iLN}{2\eta_iq} \right) (a^2 + b^2), \quad (80)$$

442 where a and b are functions of q taken from the re-scaled numerical results for stable solutions. As can be

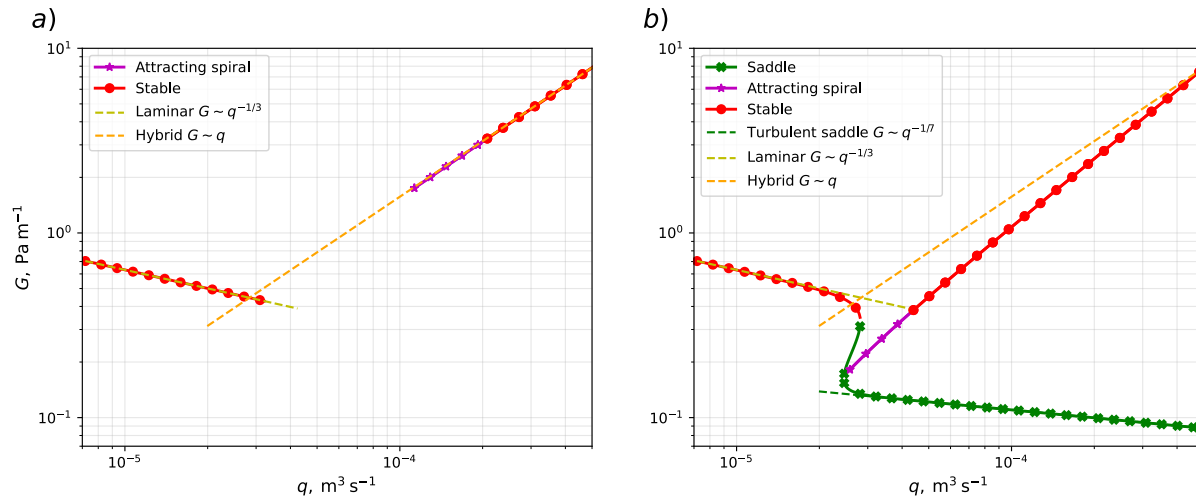


Fig. 9. Numerically derived solution to the relation between the pressure gradient, G , and the volume flux, q , required to maintain stable channels. In (a) we see the $\sim q^{-1/3}$ behaviour for low flux with laminar flow and the $\sim q$ behaviour for stable elliptical cross-sections. The gap in q where no stable points are found is in fact filled by limit cycles, which only exist for large values in k , here $k = 0.5$. The same relation is shown for a different value of $k = 0.01$ in (b) which now also shows the saddle points. Due to the smaller k , the approximate relations between G and q don't match for large q . Qualitatively, however, the curve retains a positive gradient and hence similar dynamics in a hydrological network. For a more detailed description of the effects of k see the appendix. The parameters used here are $\eta_w \sim 10^{-3}$ Pa s, $\eta_i \sim 10^{15}$ Pa s, $\rho_w \sim \rho_i \sim 10^3$ kg m $^{-3}$, $L \sim 10^5$ J kg $^{-1}$ and $N \sim 10^6$ Pa with $Re_c = 10^3$ and $f_D = 10^{-3}$.

443 seen in Fig. (9) for low flux we recover the laminar scaling $G \sim q^{-1/3}$. For large enough flux, where the
 444 hybridised cross-sections are stable, the log-log plot signifies a positive exponent in the $G(q)$ relationship.
 445 We derive this exponent using the rescaled approximation found in (77) to be $G \sim Nq$. Under conditions
 446 of constant pressure gradient this is equivalent to $N \sim q^{-1}$, similar to the behaviour predicted for canals.
 447 These relations can be understood if we consider that for large fluxes we expect stability only to be found
 448 for channels with thin and long cross-sections with near Hele-Shaw flow. As the flux is increased, in order
 449 for the flow to remain near the critical Reynolds number, the channel must become thinner, which in turn
 450 would require a greater pressure gradient resulting in this positive slope.

451 The G vs q plot in Fig. (9) provides a framework to understand and predict the evolution of channel
 452 networks consisting of multiple stable hydrologically-interacting channels experiencing different fluxes. For
 453 large enough fluxes, the plot suggests very different behaviour. If a pair of channels with differing but large
 454 fluxes are hydrologically connected, the larger channel will instead leak water to the neighbouring smaller

455 channel, encouraging the growth of the smaller channel and the shrinkage of the larger channel. Elliptical
 456 stable channels with near critical flows therefore instead drive the hydrological system towards a state with
 457 uniform channels transporting equal fluxes, in a distributed-like network. We approximate the minimum
 458 in the G vs q plot by considering the intersection of the laminar stable branch with the hybridised stable
 459 branch, as given by (68) and (69), and therefore find that

$$q_{\text{threshold}} = \sqrt{\frac{8}{\pi}} \left(\frac{\eta_i \text{Re}_c^6 \eta_w^7}{\rho_i L N \rho_w^6} \right)^{1/4}. \quad (81)$$

460 This flux can be viewed as a threshold beyond which channels are more likely to survive since any neighbouring
 461 connected channel will leak into this minimum pressure gradient channel and drive it towards elliptical
 462 cross-sections, where flux is distributed equally. According to these simplified principles of interacting
 463 channels, a channel carrying a flux beyond $q_{\text{threshold}}$ dies only if it is connected to enough smaller channels
 464 with lower pressures and carrying less than $q_{\text{threshold}}$. There must be sufficiently many small channels so
 465 $q_{\text{threshold}}$ is not crossed in the process of gaining the dying channel's flux.

466 DISCUSSION

467 By analysing the flow profiles of water through the channels, we have been able to calculate how the
 468 distribution of melt around the ice-channel boundary is affected by the channel's aspect ratio. We introduced
 469 a hybrid laminar–turbulent melt scheme that considered the Reynolds number of the flow in the channel.
 470 Combined with the viscous collapse of the channel boundary, we investigated the stability of these channels
 471 in the laminar, turbulent and near critical flow regimes. The hybrid melt scheme finds stable cross-sections
 472 in all flow regimes. For low fluxes, laminar circular cross-sections are permitted. For higher fluxes, the
 473 turbulent stationary point is a saddle, and instead we find elliptical cross-sections for channels with flow
 474 near the critical Reynolds number.

475 Limitations and Extensions

476 The relationships between G and q and the subsequent conclusions drawn from these relations rely on the
 477 assumption that the channels are in a stable state under constant flux conditions. However, the glacial
 478 melt-water flux is variable due to annual and diurnal melt-cycles (Hubbard and others, 1995). A very large
 479 change in flux over the course of just a few days is also possible due to sudden glacial lake outburst floods

(Bj rnsson, 1992), for example. We can compare the timescales of these rapid events to the timescale for channel equilibration, $\sim \eta_i/N$, which ranges from days to years depending on the local effective pressure and effective ice viscosity. We note that as in Meyer and others (2016) a strongly sheared basal ice may have a lower viscosity due to the shear-thinning ice flow-law, and hence exhibit a shorter timescale for equilibration. The timescales of flux variation and channel equilibration could therefore be comparable in these conditions. Under these circumstances, we expect subglacial channels to move a significant distance in phase space towards the stable cross-section even in response to diurnal variations, whilst other channels with longer equilibration time scales might only find stability over seasonal to annual changes in flux. Our phase portraits allow us to qualitatively consider what effect this long equilibration time might have on channels experiencing rapid changes in flux. For example, if the flow through an initially laminar and circular channel becomes turbulent due to a sudden increase in flux, the cross-section will begin to drift towards eccentricity, until either the channel becomes thin enough for the flow to become critical or, if the flux is sufficiently reduced, the flow becomes laminar and begins to drift towards a circular cross-section once more.

Throughout this work, we have considered only channels with elliptical cross-sections. This is a first generalisation away from circular channel cross-sections, introducing an additional free variable; the aspect ratio. Ellipses provide a convenient choice, as this makes the laminar flow and its temperature field solution an analytically tractable problem. Ellipses are also stable solutions to the free-boundary viscous collapse problem (Dallaston and Hewitt, 2014). An investigation into the stability of these ellipses under the hybridised melt scheme would require more computationally intensive numerical methods in order to resolve the effects of localised laminar flow on small perturbations to the interface. Direct observational evidence suggests that channel cross-sections do show roughness, with features on a range of length scales (Kamintzis and others, 2023; Church and others, 2020). Future work could examine short-wavelength instabilities at the boundary of an elliptical channel.

In this work, we assumed a Newtonian rheology for the ice, despite the known shear-thinning behaviour of ice (Glen, 1952; Goldsby and Kohlstedt, 2001; Millstein and others, 2022). This results in a closed-form expression for the viscous collapse rate. To model the collapse and evolution of an elliptical channel cross-section for a power-law rheology would require further numerical methods and is beyond the scope of this work. Given the high effective pressures driving creep closure and low flow rates, we might expect only a minor quantitative difference in behaviour (Dallaston and Hewitt, 2014). However, if viscosity changes

510 with depth around the channel profile (Meyer and others, 2016), then more complex dynamics may occur.
511 This would then necessitate the consideration of spatial variations in both the melt rate along the boundary
512 and in the closure rate due to changing viscosity.

513 **Implications for Subglacial Channels**

514 The models of englacial channels are often generalised to describe subglacial channels in contact with the
515 subglacial surface (e.g. bedrock or till) by using symmetry arguments (Fowler and Ng, 1996; Röthlisberger,
516 1972). So whilst channels experience a different boundary condition and increased resistance to flow (due
517 to a changed hydraulic diameter) at their base, we might expect similar dynamics to occur, with laminar
518 melt allowing for the existence of non-semicircular cross-sections. Observations of eskers — the remnants of
519 subglacial channels found on the exposed beds of palaeo-ice sheets — show a range of aspect ratios that
520 analyses of the flow regime (such as this) may be able to connect to the flow conditions under which they
521 formed (Schumm, 1963; Storrar and others, 2014; Hewitt and Creyts, 2019).

522 The current work may also have implications for large scale drainage network models which span a
523 glacial catchment area. A persistent challenge in continuum subglacial models attempting to predict the
524 onset and evolution of channels is the presence of small-wavelength instabilities (Hewitt, 2011; Sommers
525 and others, 2018), whereby in classical models a small perturbation to the sheet thickness is unstable
526 and prone to collapse into unphysically narrow and tall channels. Our results motivate the inclusion of
527 sidewall melting to regularise this behaviour, in a similar manner to the transverse heat diffusion recently
528 introduced by Warburton and others (2024). This work provides a related but alternative explanation,
529 whereby a narrowing channel is eventually subject to laminar-like flow with a strong tendency to melt into
530 less eccentric cross-sections, halting the instability leading to infinite aspect ratio channels, and providing a
531 physical limit to channel eccentricity. This could be used to address the persistent challenge of grid-size
532 sensitivity found in continuum subglacial models by providing a physically grounded basis for a sub-grid
533 parametrisation or a minimum grid-size, potentially removing the need for artificial numerical stabilisation.

534 Furthermore, the $G(N, q)$ relations provide a separate framework that has the potential to more simply
535 characterise and predict subglacial network growth. The GlaDS model, for instance, evolves channel
536 cross-sectional area based on standard circular Röthlisberger theory (Werder and others, 2013). Including
537 our $G(N, q)$ relations for elliptical geometries serves as a relatively simple extension. By replacing the
538 circular assumption with our elliptical relations, GlaDS could potentially capture the evolution of channels

539 in environments where high eccentricity is expected more accurately, without a significant increase in
540 computational cost.

541 CONCLUSION

542 In conclusion, we have extended Röthlisberger's theory of englacial channel evolution through melt and
543 viscous collapse by allowing for elliptical englacial channels with evolving aspect ratios and considering melt
544 from laminar, turbulent and a hybrid laminar–turbulent melt model. The viscous collapse of ice was found
545 to drive channels away from circular cross-sections toward increasingly eccentric ellipses. Melt produced by
546 viscous dissipation in purely laminar flow provides spatially variable melting along the channel walls, which
547 results in a strong forcing toward circular cross-sections. In a hybrid turbulent laminar flow model, there
548 exist non-circular channel geometries. The inclusion of both flow regimes allowed us to construct a life-cycle
549 for a channel experiencing a constant flux, in which an initially near-circular turbulent channel deforms
550 into an increasingly eccentric ellipse until local variations in melt rate along the boundary predicted by the
551 hybridised melt model stabilise the channel shape.

552 ACKNOWLEDGEMENTS

553 I.P.B is jointly and equally supported by Vice Chancellor's Award University of Cambridge and the Engi-
554 neering and Physical Sciences Research Council Doctoral Training Partnership (grant no. EP/W524633/1).
555 K.L.P.W. is funded by a Junior Research Fellowship from Trinity College, Cambridge. The authors are
556 grateful to the anonymous reviewers for their insightful comments and to the editor, all of which helped
557 improve the quality of this study.

558 REFERENCES

- 559 Björnsson H (1992) Jökulhlaups in Iceland: prediction, characteristics and simulation. *Ann. Glaciol.*, **16**, 95–106,
560 ISSN 0260-3055, 1727-5644 (doi: 10.3189/1992AoG16-1-95-106)
- 561 Bougamont M, Christoffersen P, Hubbard AL, Fitzpatrick AA, Doyle SH and Carter SP (2014) Sensitive response of
562 the Greenland ice sheet to surface melt drainage over a soft bed. *Nat. Commun.*, **5**(1), 5052, ISSN 2041-1723 (doi:
563 10.1038/ncomms6052)
- 564 Church G, Grab M, Schmelzbach C, Bauder A and Maurer H (2020) Monitoring the seasonal changes of an englacial

- 565 conduit network using repeated ground-penetrating radar measurements. *Cryosphere*, **14**(10), 3269–3286, ISSN
566 1994-0416 (doi: 10.5194/tc-14-3269-2020)
- 567 Churchill S (1977) Friction factor equations spans all fluid-flow regimes. *Chem. Eng. J.*, **84**, 91–92
- 568 Clarke GK (1987) A short history of scientific investigations on glaciers. *J. Glaciol.*, **33**(S1), 4–24, ISSN 0022-1430,
569 1727-5652 (doi: 10.3189/S0022143000215785)
- 570 Cuffey KM and Paterson WSB (2010) *The physics of glaciers*. Academic Press
- 571 Dallaston MC and Hewitt IJ (2014) Free-boundary models of a meltwater conduit. *Phys. Fluids*, **26**(8), ISSN 1070-6631,
572 1089-7666 (doi: 10.1063/1.4892389)
- 573 De Fleurian B, Werder MA, Beyer S, Brinkerhoff DJ, Delaney I, Dow CF, Downs J, Gagliardini O, Hoffman MJ,
574 Hooke RL, Seguinot J and Sommers AN (2018) SHMIP The subglacial hydrology model intercomparison project. *J.*
575 *Glaciol.*, **64**(248), 897–916, ISSN 0022-1430, 1727-5652 (doi: 10.1017/jog.2018.78)
- 576 DeConto RM and Pollard D (2016) Contribution of Antarctica to past and future sea-level rise. *Nature*, **531**(7596),
577 591–597, ISSN 0028-0836, 1476-4687 (doi: 10.1038/nature17145)
- 578 Ehrenfeucht S, Dow C, McArthur K, Morlighem M and McCormack FS (2025) Antarctic wide subglacial hydrology
579 modeling. *Geophys. Res. Lett.*, **52**(1), ISSN 1944-8007 (doi: 10.1029/2024GL111386)
- 580 Feldmann J and Levermann A (2015) Collapse of the west Antarctic ice sheet after local destabilization of the Amundsen
581 basin. *Proc. Natl. Acad. Sci.*, **112**(46), 14191–14196, ISSN 0027-8424, 1091-6490 (doi: 10.1073/pnas.1512482112)
- 582 Flowers GE (2015) Modelling water flow under glaciers and ice sheets. *Proc. Roy. Soc.*, **471** (doi:
583 10.1098/rspa.2014.0907)
- 584 Fowler AC and Ng FSL (1996) The role of sediment transport in the mechanics of jökulhlaups. *Ann. Glaciol.*, **22**,
585 255–259, ISSN 0260-3055, 1727-5644 (doi: 10.3189/1996AoG22-1-255-259)
- 586 Glen JW (1952) Experiments on the deformation of ice. *J. Glaciol.*, **2**(12), 111–114, ISSN 0022-1430, 1727-5652 (doi:
587 10.3189/S0022143000034067)
- 588 Goldsby DL and Kohlstedt DL (2001) Superplastic deformation of ice: experimental observations. *J. Geophys. Res.*
589 *Solid Earth*, **106**(B6), 11017–11030, ISSN 2156-2202 (doi: 10.1029/2000JB900336)
- 590 Happel J and Brenner H (1983) *Low Reynolds number hydrodynamics with special applications to particulate media*.
591 Martinus Nijhoff Publishers, The Hague, ISBN 90-247-2877-0
- 592 Hewitt DR, Chini GP and Neufeld JA (2018) The influence of a poroelastic till on rapid subglacial flooding and cavity
593 formation. *J. Fluid Mech.*, **855**, 1170–1207, ISSN 0022-1120, 1469-7645 (doi: 10.1017/jfm.2018.624)

- 594 Hewitt IJ (2011) Modelling distributed and channelized subglacial drainage: the spacing of channels. *J. Glaciol.*,
595 **57**(202), 302–314, ISSN 0022-1430, 1727-5652 (doi: 10.3189/002214311796405951)
- 596 Hewitt IJ (2013) Seasonal changes in ice sheet motion due to melt water lubrication. *Earth Planet. Sci. Lett.*, **371-372**,
597 16–25, ISSN 0012821X (doi: 10.1016/j.epsl.2013.04.022)
- 598 Hewitt IJ and Creyts TT (2019) A model for the formation of eskers. *Geophys. Res. Lett.*, **46**(12), 6673–6680 (doi:
599 10.1029/2019GL082304)
- 600 Hooke RL, Laumann T and Kohler J (1990) Subglacial water pressures and the shape of subglacial conduits. *J.*
601 *Glaciol.*, **36**(122), 67–71, ISSN 0022-1430, 1727-5652 (doi: 10.3189/S0022143000005566)
- 602 Hubbard BP, Sharp MJ, Willis IC, Nielsen MK and Smart CC (1995) Borehole water-level variations and the structure
603 of the subglacial hydrological system of Haut Glacier d’Arolla, Valais, Switzerland. *J. Glaciol.*, **41**(139), 572–583,
604 ISSN 0022-1430, 1727-5652 (doi: 10.3189/S0022143000034894)
- 605 Iken A and Bindschadler RA (1986) Combined measurements of subglacial water pressure and surface velocity of
606 Findelengletscher, Switzerland: conclusions about drainage system and sliding mechanism. *J. Glaciol.*, **32**(110),
607 101–119, ISSN 0022-1430, 1727-5652 (doi: 10.3189/S0022143000006936)
- 608 Kamintzis JE, Irvine-Fynn TDL, Holt TO, Jones JPP, Porter PR, Jennings SJA, Naegeli K and Hubbard B (2023)
609 Morphology, flow dynamics and evolution of englacial conduits in cold ice. *Earth Surf. Process. Landf.*, **48**(2),
610 415–432, ISSN 1096-9837 (doi: 10.1002/esp.5494)
- 611 Kazmierczak E, Gregov T, Coulon V and Pattyn F (2024) A fast and simplified subglacial hydrological model for the
612 antarctic ice sheet and outlet glaciers. *Cryosphere*, **18**(12), 5887–5911 (doi: 10.5194/tc-18-5887-2024)
- 613 Landau LD and Lifshitz EM (1987) *Fluid Mechanics*, volume 6 of *Course of theoretical physics*. Pergamon Press,
614 Oxford, 2 edition, ISBN 0-08-033933-6
- 615 Meyer CR, Fernandes MC, Creyts TT and Rice JR (2016) Effects of ice deformation on Röthlisberger channels and
616 implications for transitions in subglacial hydrology. *J. Glaciol.*, **62**(234), 750–762, ISSN 0022-1430, 1727-5652 (doi:
617 10.1017/jog.2016.65)
- 618 Millstein JD, Minchew BM and Pegler SS (2022) Ice viscosity is more sensitive to stress than commonly assumed.
619 *Commun. Earth Environ.*, **3**(1), 57, ISSN 2662-4435 (doi: 10.1038/s43247-022-00385-x)
- 620 Mouginot J, Rignot E, Björk AA, Van Den Broeke M, Millan R, Morlighem M, Noël B, Scheuchl B and Wood M
621 (2019) Forty-six years of Greenland ice sheet mass balance from 1972 to 2018. *Proc. Natl. Acad. Sci.*, **116**(19),
622 9239–9244, ISSN 0027-8424, 1091-6490 (doi: 10.1073/pnas.1904242116)

- 623 Ng FS (2000) Canals under sediment-based ice sheets. *Ann. Glaciol.*, **30**, 146–152 (doi: 10.3189/172756400781820633)
- 624 Nye JF (1953) The flow law of ice from measurements in glacier tunnels, laboratory experiments and the Jungfraufirn
625 borehole experiment. *Proc. Roy. Soc.*, **219**(1139), 477–489, ISSN 0080-4630
- 626 Pörtner HO, Roberts D, Masson-Delmotte V, Zhai P, Tignor M, Poloczanska E, Mintenbeck K, Alegría A, Nicolai M,
627 Okem A, Petzold J, Rama B and Weyer N (2019) IPCC Special Report on the Ocean and Cryosphere in a Changing
628 Climate. Technical report, United Nations Environment Programme, Cambridge, UK and New York, NY, USA
- 629 Reynolds O (1874) On the extent and action of the heating surface of stream boilers. *Proc. Lit. Soc. Manchester*, **14**,
630 7–12
- 631 Röthlisberger H (1972) Water pressure in intra- and subglacial channels. *J. Glaciol.*, **11**(62), 177–203, ISSN 0022-1430,
632 1727-5652 (doi: 10.3189/S0022143000022188)
- 633 Schlichting H and Gersten K (2017) *Boundary-Layer Theory*. Springer Berlin Heidelberg, ISBN 978-3-662-52917-1
634 978-3-662-52919-5 (doi: 10.1007/978-3-662-52919-5)
- 635 Schoof C (2010) Ice-sheet acceleration driven by melt supply variability. *Nature*, **468**(7325), 803–806, ISSN 0028-0836,
636 1476-4687 (doi: 10.1038/nature09618)
- 637 Schumm SA (1963) Sinuosity of alluvial rivers on the great plains. *Geol. Soc. Am. Bull.*, **74**(9), 1089, ISSN 0016-7606
638 (doi: 10.1130/0016-7606(1963)74[1089:SOAROT]2.0.CO;2)
- 639 Sommers A, Rajaram H and Morlighem M (2018) SHAKTI: subglacial hydrology and kinetic, transient interactions
640 v1.0. *Geosci. Model Dev.*, **11**(7), 2955–2974, ISSN 1991-959X (doi: 10.5194/gmd-11-2955-2018)
- 641 Sommers AN, Meyer CR, Poinar K, Mejia J, Morlighem M, Rajaram H, Warburton KLP and Chu W (2024) Velocity
642 of Greenland's Helheim glacier controlled both by terminus effects and subglacial hydrology with distinct realms of
643 influence. *Geophys. Res. Lett.*, **51**(15), ISSN 1944-8007 (doi: 10.1029/2024GL109168)
- 644 Storrar RD, Stokes CR and Evans DJ (2014) Morphometry and pattern of a large sample (>20,000) of Canadian
645 eskers and implications for subglacial drainage beneath ice sheets. *Quat. Sci. Rev.*, **105**, 1–25, ISSN 02773791 (doi:
646 10.1016/j.quascirev.2014.09.013)
- 647 Walder JS (2010) Röthlisberger channel theory: its origins and consequences. *J. Glaciol.*, **56**(200), 1079–1086, ISSN
648 0022-1430, 1727-5652 (doi: 10.3189/002214311796406031)
- 649 Walder JS and Fowler A (1994) Channelized subglacial drainage over a deformable bed. *J. Glaciol.*, **40**(134), 3–15,
650 ISSN 0022-1430, 1727-5652 (doi: 10.3189/S0022143000003750)

- 651 Warburton KLP, Meyer C and Sommers AN (2024) Predicting the Onset of Subglacial Drainage Channels. *J. Geophys.*
 652 *Res. Earth Surf.* (doi: 10.1029/2024jf007758)
- 653 Weisbach J (1850) *Lehrbuch der Ingenieur- und Maschinen-Mechanik*. F. Vieweg und Sohn
- 654 Werder MA, Hewitt IJ, Schoof CG and Flowers GE (2013) Modeling channelized and distributed subglacial drainage
 655 in two dimensions. *J. Geophys. Res. Earth Surf.*, **118**(4), 2140–2158 (doi: 10.1002/jgrf.20146)
- 656 Zoet LK and Iverson NR (2020) A slip law for glaciers on deformable beds. *Science*, **368**(6486), 76–78, ISSN 0036-8075,
 657 1095-9203 (doi: 10.1126/science.aaz1183)

658 APPENDIX A: LAMINAR MELTING ELLIPSE ASSUMPTION

659 In the model described here, we have constrained the cross-sectional shape of the channel to an ellipse. The
 660 melt rates could thus be characterised using their values at only two points, (1, 0) and (0, 1), which was
 661 sufficient to define the melt rate around the entire channel perimeter. Here we briefly consider the validity
 662 of this assumption.

663 The analytic expression for $\tilde{m}_l(\tilde{y}, \tilde{z})$ in equation (30) shows that the cross-section does not remain elliptical.
 664 After a small time step, $\Delta\tilde{t}$, the newly melted interface would be given by $\tilde{y}^2 + \tilde{z}^2 - 1 - 2\tilde{m}_l(\tilde{y}, \tilde{z})\Delta\tilde{t} = 0$. We
 665 can see that since \tilde{m}_l contains quartic terms in \tilde{y} and \tilde{z} , this new interface cannot be an ellipse. A detailed
 666 model of the cross-section evolution would require a free-boundary approach similar to that of Dallaston
 667 and Hewitt (2014), but with a more involved melting term. Fig. (10) shows the deviation between the
 668 elliptical assumption and the real melted back interface.

669 This deviation away from an elliptical cross-section due to melt from laminar flow can be quantified by
 670 considering whether the amount of energy required to melt the cross-section from one ellipse into another
 671 ellipse can be provided by the viscous dissipation in the flow. If the channel did indeed remain elliptical,
 672 then we can write, as in (41)

$$qG = \rho_i L \pi (a\dot{b} + \dot{a}b). \quad (3)$$

673 This can be written purely in terms of q , using (5), so that

$$\pi \left(a \frac{db}{dt} + \frac{da}{dt} b \right) = \frac{4\pi\eta_w \xi^2 + 1}{\rho_i L \xi} \left(\frac{q}{A} \right)^2. \quad (4)$$

674 By non-dimensionalising and using $d\tilde{a}/d\tilde{t} = \tilde{m}_l^a$ and $d\tilde{b}/d\tilde{t} = \tilde{m}_l^b/\xi$, the following energetic constraint is

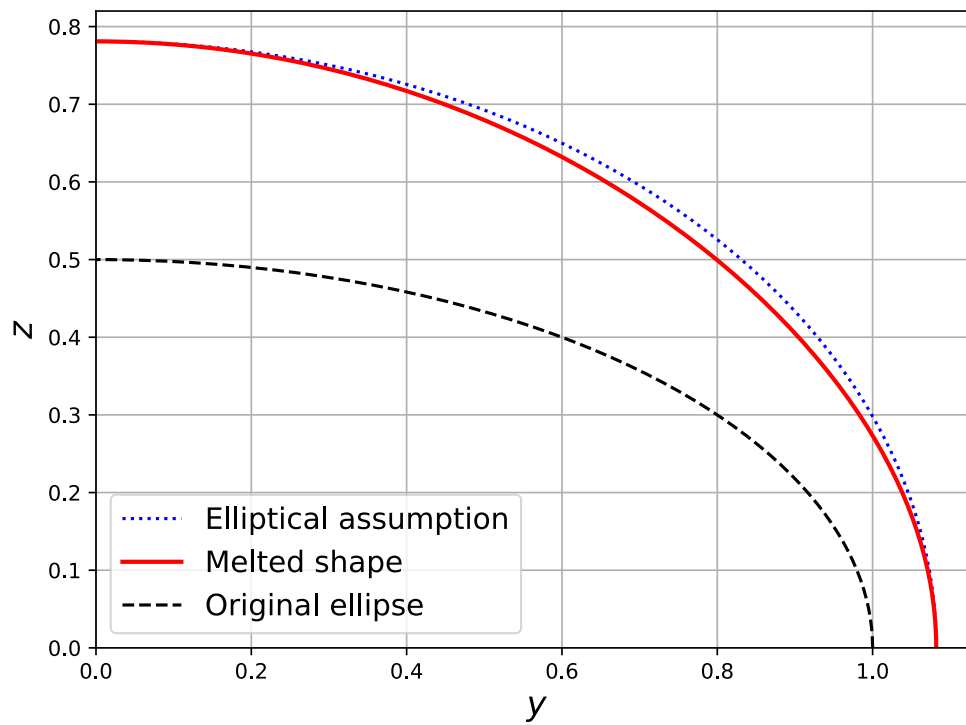


Fig. 10. Comparison between the outward melting of an elliptical boundary (solid red) and a best-fit ellipse (dotted blue) for an ellipse with $\xi = 0.5$ (dashed black), after one time step. The deviation is due to quartic terms in the melt expression \tilde{m}_l .

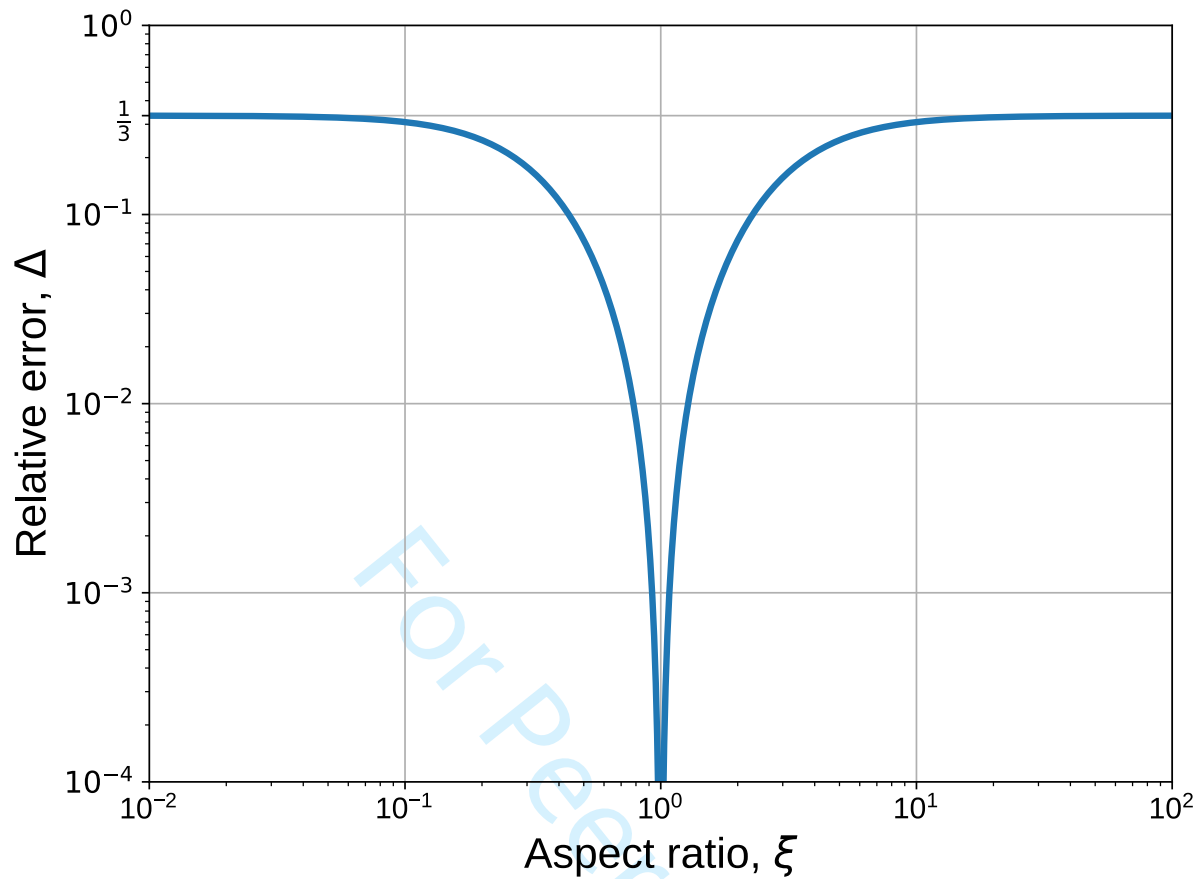


Fig. 11. The error, Δ , as defined in (6), is shown (in a log-log plot) to be at most $1/3$ and fall to zero when the aspect ratio is equal to unity.

675 placed on the axes' melt rates

$$\xi \tilde{m}_l^a + \tilde{m}_l^b = 4 \left(\xi + \frac{1}{\xi} \right). \quad (5)$$

676 However, as described in the main text, we proposed an expression for the melt rates (32) using the
 677 heat equation. When these expressions are substituted into (5) they contradict the energetic constraint,
 678 suggesting that the elliptical assumption is approximate. We quantify the deviation from the constraint by
 679 considering the relative error,

$$\Delta = \frac{\xi \tilde{m}_l^a + \tilde{m}_l^b - 4 \left(\xi + \frac{1}{\xi} \right)}{4 \left(\xi + \frac{1}{\xi} \right)}, \quad (6)$$

680 which is plotted in Fig. (11).

681 We see that in the limits of zero and infinite aspect ratio, this relative error tends to one third. Suggesting
 682 an overestimation in the melt capacity. For more reasonable aspect ratios, such as $\xi = 1/2$ this error is 7%,

683 with no error for $\xi = 1$.

684 Provided we can approximate the cross-section as elliptical, the discrepancy that results from the
685 elliptical assumption has little qualitative effect on our analysis. Firstly, the laminar stable point is found
686 at $\xi = 1$, where there is no error in the proposed forms of the melt rates. Additionally, although the hybrid
687 melt scheme may result in a quantitative overestimation of the aspect ratio of the ellipse, the error in
688 this approximation is likely significantly smaller in comparison to the assumption of the position of the
689 transition regime, defined by Re_c and k .

690 APPENDIX B: THE EFFECT OF THE TRANSITION REGION WIDTH

691 The value of k determines the size of the transition region between laminar and turbulent flow, via (45). A
692 large k and hence narrow transition region, results in stable points near to the Re_c contour in (a, b) phase
693 space. This drastically simplified the asymptotic expressions for the stable elliptical cross-sections and hence
694 the qG relations. As k increases, however, stable points for certain non-dimensional flux numbers appear to
695 vanish, this was noted in Fig. (9). Upon closer inspection, we find that these eccentric stable points lose
696 stability and becoming the centre of a limit cycle for larger k values — suggestive of a Hopf Bifurcation in
697 k space, in Fig. (12) we attach an example of such a limit cycle. For smaller values $k < 0.1$ and a wider
698 transition region, our simple asymptotic relations no longer predict the correct gradient, as can be seen in
699 Fig. (13). We note however that the gradient in the G vs q log-log plot remains positive, implying similar
700 behaviour in subglacial hydrological networks. Though of mathematical interest, the presence of limit cycles
701 is an artifact of the use of a sigmoidal function to transition between laminar and turbulent flow. A different
702 transition function may result in other dynamics, though this has not been investigated. In the context of
703 en- and subglacial channels, we expect to find attractors near the centres of these limit cycles, and so can
704 rely on the asymptotic forms given in (77), and the migration of the system towards them.

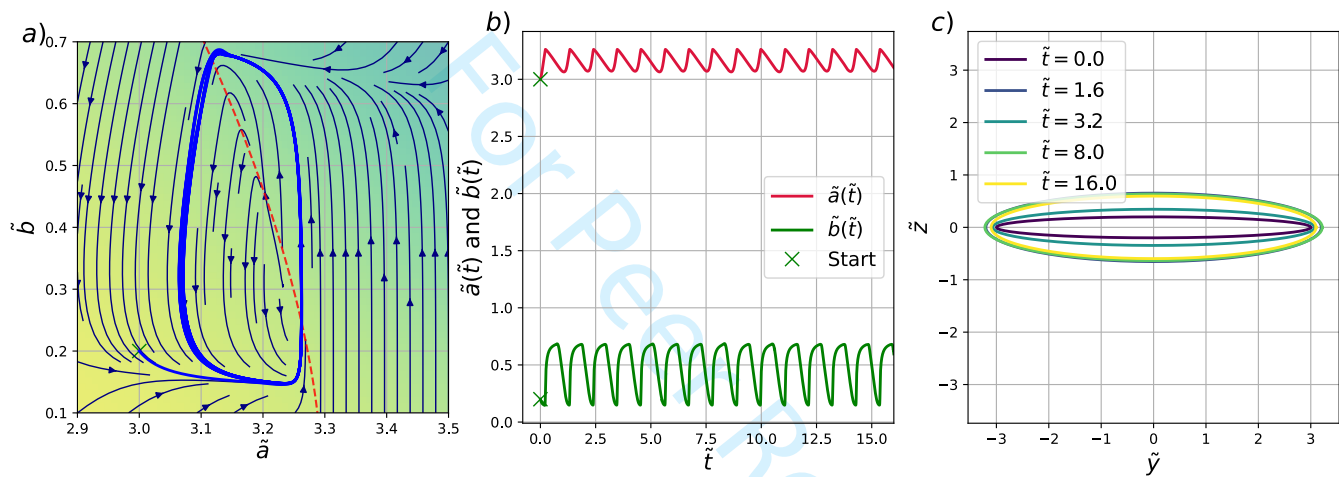


Fig. 12. Example of a limit cycle for a channel with hybridised flow and viscous closure of ice: In (a) we see the trajectory of a channel in a phase field starting at the green cross and entering a limit cycle. The red dotted line is the Re_c contour. The trajectories of the semi-axes are shown independently in (b), and snapshots of the channel cross-sections are shown in (c). The parameters used here are $k = 0.5$, $q = 6 \times 10^{-5} \text{ m}^3 \text{ s}^{-1}$, $\eta_w \sim 10^{-3} \text{ Pa s}$, $\eta_i \sim 10^{15} \text{ Pa s}$, $\rho_w \sim \rho_i \sim 10^3 \text{ kg m}^{-3}$, $L \sim 10^5 \text{ J kg}^{-1}$ and $N \sim 10^6 \text{ Pa}$ with $Re_c = 10^3$ and $f_D = 10^{-3}$.

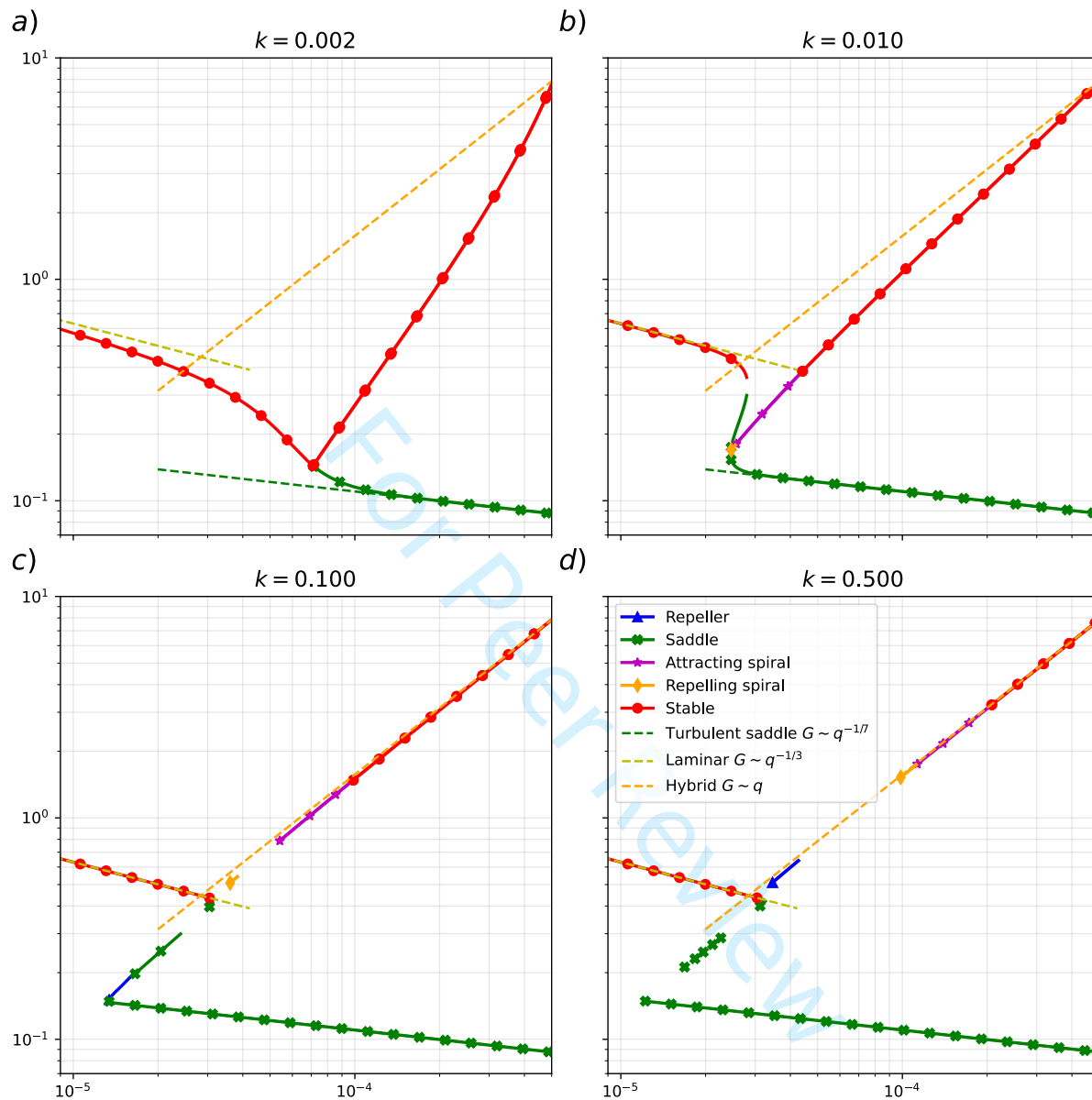


Fig. 13. Pressure-flux relations for varying transition thicknesses, governed by k : For smaller values of k and hence larger transition regions attracting stationary points exist for all fluxes, as in (a) and (b). Note that the curve of the stable points is steeper than the asymptotic hybrid line $G \sim q$, for these values of k . Figures (c) and (d) show the growth of a gap in attracting stationary points these are due to the presence of limit cycles. As the transition region decreases in size the curve of attracting stationary points adheres closely to the asymptotic solution. The parameters used here are $\eta_w \sim 10^{-3} \text{ Pa s}$, $\eta_i \sim 10^{15} \text{ Pa s}$, $\rho_w \sim \rho_i \sim 10^3 \text{ kg m}^{-3}$, $L \sim 10^5 \text{ J kg}^{-1}$ and $N \sim 10^6 \text{ Pa}$ with $\text{Re}_c = 10^3$ and $f_D = 10^{-3}$.